

TOPICAL REVIEW

Multiscale modeling and general theory of non-equilibrium plasma-assisted ignition and combustion

To cite this article: Suo Yang *et al* 2017 *J. Phys. D: Appl. Phys.* **50** 433001

View the [article online](#) for updates and enhancements.

Topical Review

Multiscale modeling and general theory of non-equilibrium plasma-assisted ignition and combustion

Suo Yang¹, Sharath Nagaraja¹, Wenting Sun¹ and Vigor Yang^{1,2}

¹ School of Aerospace Engineering, Georgia Institute of Technology, Atlanta, GA 30332, United States of America

E-mail: syang305@gatech.edu, bn.sharath@gmail.com, wenting.sun@aerospace.gatech.edu and vigor.yang@aerospace.gatech.edu

Received 28 June 2017, revised 20 August 2017

Accepted for publication 23 August 2017

Published 26 September 2017



CrossMark

Abstract

A self-consistent framework for modeling and simulations of plasma-assisted ignition and combustion is established. In this framework, a ‘frozen electric field’ modeling approach is applied to take advantage of the quasi-periodic behaviors of the electrical characteristics to avoid the re-calculation of electric field for each pulse. The correlated dynamic adaptive chemistry (CO-DAC) method is employed to accelerate the calculation of large and stiff chemical mechanisms. The time-step is dynamically updated during the simulation through a three-stage multi-time scale modeling strategy, which utilizes the large separation of time scales in nanosecond pulsed plasma discharges. A general theory of plasma-assisted ignition and combustion is then proposed. Nanosecond pulsed plasma discharges for ignition and combustion can be divided into four stages. Stage I is the discharge pulse, with time scales of O (1–10 ns). In this stage, input energy is coupled into electron impact excitation and dissociation reactions to generate charged/excited species and radicals. Stage II is the afterglow during the gap between two adjacent pulses, with time scales of O (100 ns). In this stage, quenching of excited species dissociates O₂ and fuel molecules, and provides fast gas heating. Stage III is the remaining gap between pulses, with time scales of O (1–100 μs). The radicals generated during Stages I and II significantly enhance exothermic reactions in this stage. The cumulative effects of multiple pulses is seen in Stage IV, with time scales of O (1–1000 ms), which include preheated gas temperatures and a large pool of radicals and fuel fragments to trigger ignition. For flames, plasma could significantly enhance the radical generation and gas heating in the pre-heat zone, thereby enhancing the flame establishment.

Keywords: plasma fluid modeling, nanosecond plasma discharge, ignition, plasma-assisted combustion, low-temperature chemistry

(Some figures may appear in colour only in the online journal)

Contents

Nomenclature	2	2.2. Governing equations	4
1. Introduction	3	2.3. Boundary conditions	5
2. Theoretical framework	3	2.4. Necessity for one- and multi-dimensional modeling	5
2.1. Physical configurations	3	2.5. Plasma-combustion chemistry	6
		3. Numerical modeling strategies	6
		3.1. ‘Frozen electric field’ strategy	6

² Author to whom any correspondence should be addressed.

3.2. Correlated dynamic adaptive chemistry and transport (CO-DACT) strategy.....7

3.3. Three-stage multi-time scale modeling strategy7

4. General theory.....8

4.1. Nanosecond pulsed plasma discharges: a multi-time scale theory.....8

4.1.1. Stage I—discharge pulse8

4.1.2. Stage II—afterglow.....10

4.1.3. Stage III—remaining gap between pulses10

4.1.4. Stage IV—completion of O (1 00) pulses11

4.2. Plasma-assisted ignition.....11

4.2.1. First-stage ignition to ‘cool flame’11

4.2.2. Second-stage ignition to hot flame12

4.2.3. Ignition kernel propagation.....13

4.3. Plasma-assisted flames.....13

4.3.1. Premixed flame13

4.3.2. Non-premixed (diffusion) flame15

5. Conclusions.....15

Acknowledgments.....16

References.....16

M average molecular weight of air (kg)

m_e electron mass (kg)

N number density of neutral particles (cm^{-3})

n_s outward unit normal vector

n_e electron number density (cm^{-3})

n_k number density of the k th species (cm^{-3})

n_ϵ electron energy density ($\text{eV} \cdot \text{cm}^{-3}$)

$n_{+,-}$ sum of number densities of positive and negative ions, respectively (cm^{-3})

p pressure ($\text{kg} \cdot \text{cm}^{-1} \cdot \text{s}^{-1}$)

Q_ϵ production rate of electron energy density ($\text{eV} \cdot \text{cm}^{-3} \cdot \text{s}^{-1}$)

\dot{Q}^{JH} energy release rate from Joule heating ($\text{kg} \cdot \text{cm}^{-1} \cdot \text{s}^{-3}$)

Q_{pulse} input energy per pulse (mJ)

q_i energy flux from heat conduction and diffusion ($\text{kg} \cdot \text{s}^{-3}$)

q_k charge number of the k th species (-1 for negative ions and electrons, $+1$ for positive ions, and 0 for neutral species)

r_i reaction rate of the i th electron impact reaction ($\text{cm}^{-3} \cdot \text{s}^{-3}$)

S_L laminar flame speed ($\text{cm} \cdot \text{s}^{-1}$)

S_{ign} ignition kernel propagation speed ($\text{cm} \cdot \text{s}^{-1}$)

T gas temperature (K)

T_{amb} ambient temperature (K)

T_b boundary temperature (K)

T_e electron temperature (K)

T_{gw} gas temperature at a distance Δx from the solid wall (K)

T_{ref} reference temperature (K)

T_{se} temperature of secondary electrons ejected from the electrode surface (eV)

t_{pulse} duration of one pulse (ns)

\mathbf{u} convective velocity vector of the gas mixture ($\text{cm} \cdot \text{s}^{-1}$)

u_i, u_j flow velocity components in i th and j th directions, respectively ($\text{cm} \cdot \text{s}^{-1}$)

V_{app} applied voltage (V)

V_{gap} gap voltage (V)

V_{peak} peak value of applied voltage (kV)

γ secondary electron emission coefficient for ions colliding with electrode surface

ΔE_i heat of the i th electron impact reaction (eV)

$\Delta n_{e,\text{max}}$ maximum relative difference in the electron number density at the end of two adjacent discharge pulses

ϵ electric permittivity ($\text{F} \cdot \text{cm}^{-1}$)

ϵ_d dielectric constant

ϵ_e electron energy (eV)

κ dynamic viscosity ($\text{kg} \cdot \text{cm}^{-1} \cdot \text{s}^{-1}$)

λ thermal conductivity of the gas mixture ($\text{W} \cdot \text{cm}^2 \cdot \text{K}^{-1}$)

μ_k mobility of the k th species in the electric field ($\text{cm}^2 \cdot \text{V}^{-1} \cdot \text{s}^{-1}$)

μ_ϵ electron energy mobility ($\text{cm}^2 \cdot \text{V}^{-1} \cdot \text{s}^{-1}$)

ν_{el} elastic collision frequency of electrons (s^{-1})

ρ density of the plasma mixture ($\text{kg} \cdot \text{cm}^{-3}$)

Nomenclature

$C_{p,k}$ specific heat at constant pressure of the k th species ($\text{J} \cdot \text{kg}^{-1} \cdot \text{K}^{-1}$)

D_k effective diffusion coefficient of the k th species ($\text{cm}^2 \cdot \text{s}^{-1}$)

D_ϵ electron energy diffusion coefficient ($\text{cm}^2 \cdot \text{s}^{-1}$)

Dec_k decay rate of the k th species ($\text{kg} \cdot \text{cm}^{-3} \cdot \text{s}^{-1}$)

E electric field ($\text{V} \cdot \text{cm}^{-1}$)

E total energy ($\text{J} \cdot \text{kg}^{-1}$)

E/N reduced electric field (Td)

F_i^{EHD} electro-hydrodynamic force per unit volume ($\text{kg} \cdot \text{cm}^{-2} \cdot \text{s}^{-1}$)

$G(t)$ non-dimensional heat transfer parameter

h gas mixture enthalpy ($\text{J} \cdot \text{kg}^{-1}$)

h_k^0 enthalpy of formation of the k th species at T_{ref} ($\text{J} \cdot \text{kg}^{-1}$)

J_e electron density flux ($\text{cm}^{-2} \cdot \text{s}^{-1}$)

$J_{e,s}$ wall boundary flux of electrons ($\text{cm}^{-2} \cdot \text{s}^{-1}$)

J_k flux of the k th species ($\text{cm}^{-2} \cdot \text{s}^{-1}$)

J_ϵ flux of electron energy ($\text{eV} \cdot \text{cm}^{-2} \cdot \text{s}^{-1}$)

$J_{\epsilon,s}$ wall boundary flux of electron energy ($\text{eV} \cdot \text{cm}^{-2} \cdot \text{s}^{-1}$)

$J_{+,-}$ net positive and negative charge fluxes, respectively ($\text{cm}^{-2} \cdot \text{s}^{-1}$)

$J_{+,s}$ wall boundary flux of positive ions ($\text{cm}^{-2} \cdot \text{s}^{-1}$)

$J_{-,s}$ wall boundary flux of negative ions ($\text{cm}^{-2} \cdot \text{s}^{-1}$)

k_d thermal conductivity of quartz ($\text{W} \cdot \text{m}^{-1} \cdot \text{K}^{-1}$)

k_{gw} thermal conductivity of the gas mixture at temperature T_{gw} ($\text{W} \cdot \text{m}^{-1} \cdot \text{K}^{-1}$)

L gap length (cm)

l_d thickness of the dielectric layer (cm)

τ_{ij}	viscous shear stress tensor ($\text{kg} \cdot \text{cm}^{-1} \cdot \text{s}^{-2}$)
τ_{plasma}	ignition delay after plasma pulse burst (s)
τ_{self}	auto-ignition delay without plasma (s)
ϕ	electric potential (V)
$\dot{\omega}_k$	production term of the k th species ($\text{cm}^{-3} \cdot \text{s}^{-1}$)

1. Introduction

Over the past decade, non-equilibrium plasma has been the subject of significant attention, due to its great potential to enhance ignition and combustion in internal combustion engines, gas turbines, scramjet engines, and pulsed detonation engines [1, 2]. Past studies have shown that nanosecond discharge plasma can shorten ignition delays [3, 4], extend the flammability limits to allow ultra-lean combustion for emission reduction [5], increase flame propagation speed [6, 7], and improve flame stabilization [8]. Despite promising results, the underlying physio-chemical processes for such enhancement are still not well understood.

The existing experimental studies can be divided into two categories. The first category attempts to study plasma-assisted combustion in complex flow environments representative of real engine combustors. For example, Zhang *et al* [9, 10] studied the interaction between a plasma jet and turbulent flow; Kim *et al* [11] investigated the effect of plasma on a fuel jet in cross flow; Starikovskaia *et al* [12] and Leonov *et al* [13, 14] examined the interaction between plasma and supersonic combustion. The complex flow structures in these experiments confounded the fundamental plasma enhancement mechanisms. In the second category, experiments are conducted in canonical configurations to simplify or even eliminate hydrodynamic effects and isolate plasma enhancement from other effects. For example, Uddi *et al* [15] conducted two-photon absorption laser induced fluorescence (TALIF) measurements of atomic oxygen in fuel/air mixtures subject to nanosecond pulsed discharges in a rectangular quartz reactor. Yin *et al* [16] studied the ignition of mildly preheated H_2/air mixtures under nanosecond pulsed discharges in a quartz flow reactor. Lefkowitz *et al* [17] conducted *in situ* measurements of nanosecond pulsed plasma activated $\text{C}_2\text{H}_4/\text{Ar}$ pyrolysis and oxidation of $\text{C}_2\text{H}_4/\text{O}_2/\text{Ar}$ mixtures in a flow reactor.

Although this second category of experimental studies provides more insights into the underlying physio-chemical processes of plasma enhancement, the number of measurable quantities remains limited and many conclusions are indirectly inferred. For this reason, high-fidelity modeling and simulations of plasma-assisted ignition and combustion are vital. Comprehensive numerical models of plasma have been developed over the last several decades, and the field is relatively mature. For example, Ventzek *et al* [18] developed a high dimensional plasma model, and Shigeta [19] reviewed a class of models for plasma-turbulence interaction. In contrast, the modeling of plasma-assisted ignition and combustion appears to be limited, primarily because the range of scales involved makes the computation extremely challenging. In addition, most of these studies [20–22] are zero-dimensional (0D), due to the complexity of plasma-combustion interaction. In 0D models, plasma discharges

are assumed to be uniform over the entire domain during each pulse, and the influence of cathode sheath formation is neglected. Furthermore, because the energy input channels are difficult to model in 0D models, the reduced electric field (E/N) and electron density are pre-specified such that the coupled energy can match experimentally measured values. To address these issues, our group has developed a self-consistent, one-dimensional (1D) model [23–25] for taking into account various spatiotemporal scales involved in plasma-assisted ignition and combustion. This model resolves the transient electric field during each nanosecond discharge pulse, and calculates the cumulative effects of multiple pulses on fuel dissociation/pyrolysis, oxidation, ignition, and combustion. The work has been extensively validated in three typical configurations for a wide range of fuel types and operating conditions [26–30]. In the first half of this paper, we will summarize the different modeling strategies we have developed over the past decade.

There have been several topic reviews for the field of plasma-assisted ignition and combustion in recent years. Starikovskaia [12] and Starikovskii *et al* [31] summarized the discharge types, and evaluated the oxidation of different hydrocarbons by nanosecond discharge and the control of their ignition and combustion characteristics. Starikovskii and Aleksandrov [1] reviewed the applications and physics of plasma-assisted combustion. Sun and Ju [32–34] reviewed the chemical kinetics and diagnostics of plasma-assisted low-temperature combustion. The present paper focuses on numerical modeling and attempts to develop a general multi-time scale theory of plasma-assisted ignition and combustion.

The structure of this paper is as follows. Section 2 reviews a self-consistent theoretical framework for plasma-assisted ignition and combustion. Section 3 summarizes the different modeling strategies. Finally, section 4 develops a general theory for nanosecond plasma discharges, plasma-assisted ignition, and plasma-assisted premixed and non-premixed flames.

2. Theoretical framework

This section covers the physical configurations under consideration, the governing equations and their boundary conditions, the necessity for at least 1D modeling, and plasma-combustion chemistry.

2.1. Physical configurations

Three configurations are considered to study the effects of non-equilibrium plasma discharges on ignition, premixed flames, and non-premixed flames.

The first configuration [23, 27, 29, 30], shown in figure 1(a), is designed to simulate plasma discharges of fuel/oxidizer/diluent mixtures for low-temperature fuel oxidation and ignition. It is a plane-to-plane geometry to mimic nanosecond dielectric barrier discharge (NS DBD) reactor experiments [16, 17, 30, 35]. Two copper electrodes coated by thin dielectric layers are placed 1–1.5 cm apart, with the gap between them filled with gas mixtures. A high voltage power supply is connected to the right electrode, while the left electrode is grounded.

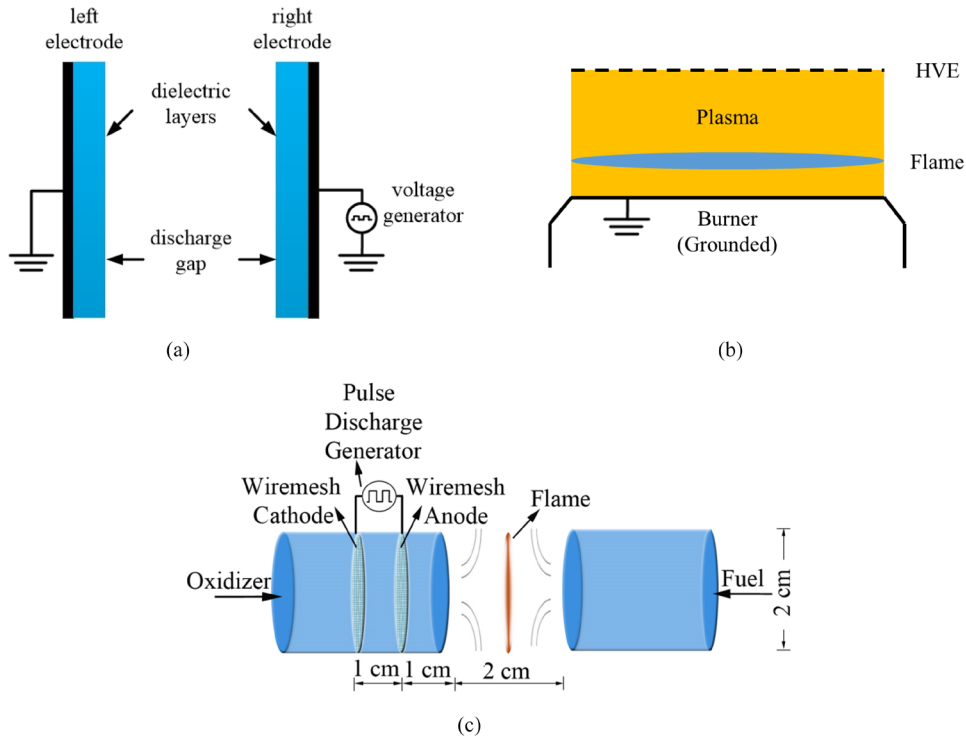


Figure 1. (a) Schematic of plane-to-plane simulation configuration [23, 27, 29, 30]. Reproduced from [23]. © IOP Publishing Ltd. All rights reserved. (b) Schematic of the ‘direct coupling’ flat premixed flame configuration [28]. Reprinted from [28], Copyright 2015, with permission from Elsevier. (c) Schematic of counter-flow non-premixed flame configuration [26].

The second configuration [28], shown in figure 1(b), treats a plasma-assisted laminar flat premixed flame, simulating the McKenna burner experiment [36]. The entire flame is encapsulated in the plasma discharge. The burner exit serves as the ground electrode, and the high-voltage electrode, which is a perforated metal plate, is located 4 cm above the burner exit.

The third configuration [26, 37], shown in figure 1(c), simulates plasma-assisted non-premixed flames in counter-flow experiments [38]. Two wire-mesh electrodes covered with thin alumina as dielectric layer (1.5 mm in thickness) are placed 1 cm apart in a tube filled with oxidizer. In this configuration, the discharge region is separated from the oxidizer burner exit. Thus, the residence time is large enough for gas temperature and species concentration to become uniform at the cross section of the oxidizer burner exit, to support the 1D assumption in this study.

2.2. Governing equations

A two-temperature non-equilibrium plasma model is developed, in which ions and neutral species are in thermal equilibrium at the gas temperature T [39], and electrons are in thermal non-equilibrium with the electron temperature T_e approximated by the ‘local electron mean energy method’ [40]. The governing equations include the Poisson equation for electric potential, the electron energy equation, and transport equations for charged and neutral species, as equations (1)–(3), respectively:

$$\nabla \cdot (\epsilon \nabla \phi) = -e(n_+ - n_- - n_e) \quad (1)$$

$$\frac{\partial n_e}{\partial t} + \nabla \cdot J_e = \dot{Q}_e \quad (2)$$

$$\frac{\partial n_k}{\partial t} + \nabla \cdot J_k = \dot{\omega}_k. \quad (3)$$

Electric field ($\mathbf{E} = -\nabla\phi$) and energy input is thus calculated, rather than pre-specified as in the 0D models [17]. The transport of energy and species is treated using the drift (mobility)-diffusion model. The electron energy density is $n_e = n_e \epsilon_e$. The flux term \mathbf{J}_e is defined as

$$\mathbf{J}_e = -\mu_e n_e \mathbf{E} - \nabla(D_e n_e) + n_e \mathbf{u}. \quad (4)$$

The source term \dot{Q}_e is defined as

$$\dot{Q}_e = - \left(\frac{3k_B m_e}{eM} \right) n_e \nu_{el} (T_e - T) - \sum \Delta E_i r_i - \sum \mathbf{J}_e \cdot \mathbf{E}. \quad (5)$$

Here, the first term on the right-hand side represents the electron energy loss from elastic collisions with gas molecules. The second term characterizes the energy loss from electron impact reactions. The third term denotes the energy gain from the acceleration in the applied electric field. For species transport equations, the flux term \mathbf{J}_k is defined as

$$\mathbf{J}_k = q_k \mu_k n_k \mathbf{E} - \nabla(D_k n_k) + n_k \mathbf{u}. \quad (6)$$

The electron transport and reaction-rate coefficients are fitted as functions of electron energy ϵ_e calculated by solving the electron Boltzmann equation with two-term expansion using the BOLSIG software [41], and renewed by interpolation at every time step and every spatial grid-point.

The gas flow is governed by the conservation equations of mass, momentum and total energy, as equations (7)–(9), respectively:

$$\frac{\partial \rho}{\partial t} + \frac{\partial \rho u_i}{\partial x_i} = 0 \quad (7)$$

$$\frac{\partial \rho u_i}{\partial t} + \frac{\partial (\rho u_i u_j)}{\partial x_j} = -\frac{\partial p}{\partial x_i} + \frac{\partial \tau_{ij}}{\partial x_j} + F_i^{\text{EHD}} \quad (8)$$

$$\frac{\partial \rho E}{\partial t} + \frac{\partial [(\rho E + p) u_i]}{\partial x_i} = -\frac{\partial q_i}{\partial x_i} + \frac{\partial (u_i \tau_{ij})}{\partial x_j} + \dot{Q}^{\text{JH}}. \quad (9)$$

Following classical thermodynamics, the total energy ρE is defined as

$$\rho E = \rho h - p + \frac{\rho (u_i u_j)}{2} \quad (10)$$

where the mixture enthalpy is defined as

$$h = \sum_k Y_k \left\{ h_k^0(T_{\text{ref}}) + \int_{T_{\text{ref}}}^T C_{p,k}(T') dT' \right\}. \quad (11)$$

The stress tensor τ_{ij} is defined as

$$\tau_{ij} = \kappa \left(\frac{\partial u_i}{\partial x_j} + \frac{\partial u_j}{\partial x_i} \right) \quad (12)$$

and the energy flux q_i from heat conduction and species diffusion is defined as

$$q_i = -\lambda \left(\frac{\partial T}{\partial x_j} \right) + \rho \sum_k h_k Y_k D_k \left(\frac{\partial Y_k}{\partial x_j} \right). \quad (13)$$

Two special terms are introduced for plasma. The electrohydrodynamic force term F_i^{EHD} is defined as

$$F_i^{\text{EHD}} = e E_i (n_+ - n_- - n_e) \quad (14)$$

The Joule heating rate \dot{Q}^{JH} is defined as

$$\dot{Q}^{\text{JH}} = e \mathbf{E} \cdot \sum (\mathbf{J}_+ - \mathbf{J}_- - \mathbf{J}_e). \quad (15)$$

Unlike equilibrium plasma, which transfers electrical energy only into sensible enthalpy, non-equilibrium plasma transfers electrical energy into the total energy of the gas mixture, and this triggers both gas temperature rise and chemical reactions. Heat release from chemical reactions is implicitly included in the unsteady term of the total energy equation, in the form of chemical energy being converted into sensible enthalpy.

2.3. Boundary conditions

Electric potential ϕ is set to zero at the left boundary, and to the gap voltage V_{gap} at the right boundary. Gap voltage V_{gap} is calculated from the applied voltage V_{app} by solving the following equation [42]:

$$\frac{dV_{\text{app}}}{dt} = \left(1 + \frac{2l_d}{\epsilon_d L} \right) \frac{dV_{\text{gap}}}{dt} - \frac{2l_d e}{\epsilon_d \epsilon_0 L} \int_0^L [J_+ - J_-] dx. \quad (16)$$

In the simulations, as shown in figure 2, a Gaussian fit of the experimental pulse waveform is used as the applied voltage V_{app} . It is worth noting that the input pulse energy and ignition characteristics have been found to be highly sensitive to uncertainties in dielectric properties [27].

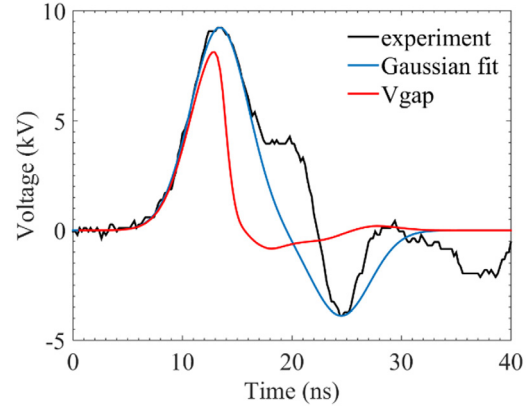


Figure 2. Example of Gaussian fit of experimental pulse waveform used in simulation [29].

Zero wall flux is enforced for all neutral species. The wall fluxes for electrons, positive ions, negative ions, and electron energy are specified by equations (17)–(20), respectively [43]:

$$\mathbf{J}_{e,s} \cdot \mathbf{n}_s = \frac{1}{4} n_e \sqrt{\frac{8k_b T_e}{\pi m_e}} + (a-1) \mu_e n_e \mathbf{E} \cdot \mathbf{n}_s - a \sum_k \gamma \mathbf{J}_{+k,s} \cdot \mathbf{n}_s \quad (17)$$

$$\mathbf{J}_{+,s} \cdot \mathbf{n}_s = \frac{1}{4} n_+ \sqrt{\frac{8k_b T_g}{\pi m_+}} + a \mu_+ n_+ \mathbf{E} \cdot \mathbf{n}_s \quad (18)$$

$$\mathbf{J}_{-,s} \cdot \mathbf{n}_s = \frac{1}{4} n_- \sqrt{\frac{8k_b T_g}{\pi m_-}} + (a-1) \mu_- n_- \mathbf{E} \cdot \mathbf{n}_s \quad (19)$$

$$\mathbf{J}_{e,s} \cdot \mathbf{n}_s = \left(\frac{5}{2} k_b T_e \right) \left[\frac{1}{4} n_e \sqrt{\frac{8k_b T_e}{\pi m_e}} + (a-1) \mu_e n_e \mathbf{E} \cdot \mathbf{n}_s \right] - a \left(\frac{5}{2} k_b T_{se} \right) \sum_k \gamma \mathbf{J}_{+k,s} \cdot \mathbf{n}_s \quad (20)$$

where the secondary electron emission coefficient γ is assumed to be 0.05 [43]. The temperature of the secondary electrons ejected from the electrode surface T_{se} is set to 1 eV [43]. In addition, $a = 1$ if $\mathbf{E} \cdot \mathbf{n}_s < 0$, and $a = 0$ otherwise.

Zero wall flux is enforced for mass and momentum equations. The gas temperature boundary condition is set to be the analytic self-similar solution of the transient temperature distribution in a semi-infinite solid with constant heat flux [44]:

$$T_b = \frac{T_{\text{amb}} + G(t) \times T_{\text{gw}}}{1 + G(t)}; G(t) = \frac{4k_{\text{gw}} \sqrt{\alpha_d t / \pi}}{k_d \Delta x}. \quad (21)$$

In practice, this boundary is closer to isothermal than to adiabatic conditions.

2.4. Necessity for one- and multi-dimensional modeling

The governing equations and boundary conditions described in the previous sections indicate that modeling must be at least 1D to capture cathode sheath formation and to calculate E/N accurately, where 0D models pre-specify it. As shown in figure 3, the sheath is the boundary between the plasma and the electrodes, with large electric field and electron number density gradients. In fact, rapid gas heating through ion Joule

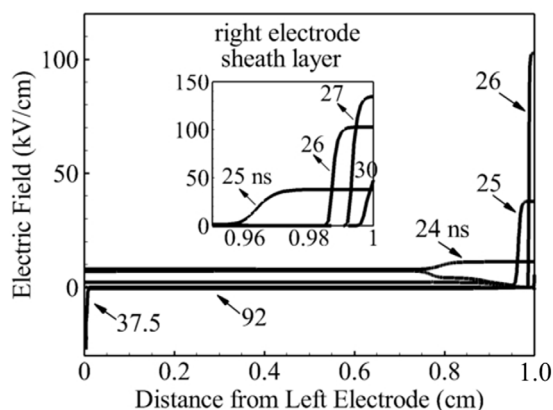


Figure 3. Spatial variation in electric field during first voltage pulse. Simulation conducted in air at 60 Torr and 300 K initial pressure and temperature, at 40 kHz repetition rate [23]. Reproduced from [23]. © IOP Publishing Ltd. All rights reserved.

effect mostly occurs inside the sheath boundary rather than in the bulk plasma [23]. Such heat addition is rapidly dissipated to the wall, because the boundary is approximately isothermal instead of adiabatic. Conductive heat loss to the walls, together with thermal diffusion into the bulk gas, prevents the overheating of the cathode sheath layer and the formation of ionization instabilities [23]. For this reason, the input energy matching in 0D models often results in over-prediction of the gas temperature of the bulk plasma.

To demonstrate the necessity of 1D modeling, Yang *et al* [29] directly compared the results from 1D and 0D models of nanosecond pulsed plasma-activated $C_2H_4/O_2/Ar$ mixtures, using the same plasma-combustion chemistry. For all quantities, the 1D model provides significantly better predictions than the 0D model, with respect to experimental measurements. Further analysis indicated that the kinetics pathways of fuel dissociation and oxidation are similar, but different pathways dominate in the two models.

2.5. Plasma-combustion chemistry

In this study, air or O_2/Ar serve as the oxidizer and diluent (background gas), and a wide range of fuels is investigated, including hydrogen (H_2), ethylene (C_2H_4), dimethyl ether (DME: CH_3OCH_3), and n-heptane (nC_7H_{16}). DME and n-heptane are hydrocarbon fuels with low-temperature (below 700–800 K) chemistry (LTC) behavior. Reaction rate constants of electron impact reactions are calculated at each spatial grid-point and time step using BOLSIG [41] and modeled as functions of electron energy ϵ_e .

The chemical kinetics models for air-plasma [23] and O_2/Ar plasma [29] are reduced from a detailed mechanism [15] via sensitivity analysis. The model includes neutral species N , N_2 , Ar , O , O_2 , O_3 , and NO ; the charged species e^- , N_2^+ , N_4^+ , Ar^+ , O_2^+ , O_4^+ , and O_2^- ; and electronically excited species $N_2(A^3\Sigma)$, $N_2(B^3\Pi)$, $N_2(C^3\Pi)$, $N_2(a^1\Sigma)$, Ar^* , $O_2(a^1\Delta)$, $O_2(b^1\Sigma)$, $O_2(c^1\Sigma)$, $N(^2D)$, and $O(^1D)$. CARS measurements of nitrogen vibrational temperature in air [20] indicated that the vibrational non-equilibrium is insignificant and not likely to affect the plasma chemistry, due to the fast vibrational relaxation within

O (10 ns) [45, 46]. Therefore, vibrational excited species are not explicitly included in the model. For electron impact reactions, self-consistent sets of electron impact cross-sections are used for O_2 [47], N_2 [48], and Ar [49]. The rate constants of reactions between Ar^* and O_2 were taken from Sun *et al* [50].

For H_2 fuel, a chemistry model [27] is reduced from the above-mentioned plasma air chemistry, classical H_2/O_2 ignition kinetics [51], and H_2 plasma reactions [52, 53] through sensitivity analysis. In addition to those species in the air-plasma chemistry, this reduced mechanism also includes neutral species H_2 , H , OH , HO_2 , and H_2O , and charged species HN_2^+ , and H_3O^+ .

For C_2H_4 fuel, the performance of two models, HP-Mech [17] and USC Mech-II [54], was compared for the prediction of nanosecond pulsed plasma activated $C_2H_4/O_2/Ar$ mixtures [29]. The predictions from HP-Mech were found to be better than those of USC Mech-II in terms of comparison with the experimental measurements, mainly because USC Mech-II does not include the high-pressure/low-temperature reaction pathway $OH + C_2H_4 \rightarrow CH_2CH_2OH$. The C_2H_4 excitation cross-sections were estimated based on Janev and Reiter's method [55].

For DME and nC_7H_{16} fuels, two chemical models [30, 56, 57] were developed based on a DME combustion model [58] and a reduced nC_7H_{16} model [59, 60]. In addition to H_2/air plasma-combustion chemistry, these mechanisms also include the charged species CH_3^+ , $CH_3OCH_2^+$, $CH_3OCH_3^+$, $C_7H_{15}^+$, $C_6H_{13}^+$, $C_5H_{11}^+$, and many neutral species. There are, however, no available cross-section data of electron impact reactions for DME and nC_7H_{16} . It is assumed that their cross-sections are similar to that of C_2H_6 [61], which has a similar molecular structure. A sensitivity analysis was conducted by varying (up to 5 times) the rate constants of electron impact and quenching reactions, and a negligible impact on ignition delay predictions was observed [56].

Past studies [62] proved that the dominant reaction pathway for atomic oxygen (O) generation is $e + O_2 = e + O + O(^1D)$, which means that almost half of the O produced by plasma is $O(^1D)$. In typical plasma-assisted ignition and combustion conditions, the high concentration of hydrocarbons result in much faster reactions between $O(^1D)$ and hydrocarbons (approximately 4 times) than the quenching of $O(^1D)$ to O [29], and should be added to the plasma-combustion chemistry models.

3. Numerical modeling strategies

The conservation equations of mass, momentum, energy, and neutral species are spatially discretized using a central scheme with the total variation diminishing (TVD) property [63]. The charged species equations derived from the drift (mobility)-diffusion model are spatially discretized using an exponential Scharfetter–Gummel scheme [64]. The numerical mesh is clustered toward the two electrodes to resolve steep gradients inside the sheath layers.

3.1. 'Frozen electric field' strategy

The 'frozen electric field' strategy takes advantage of the quasi-periodic behaviors of the electrical field to avoid recalculating the electric field for each pulse.

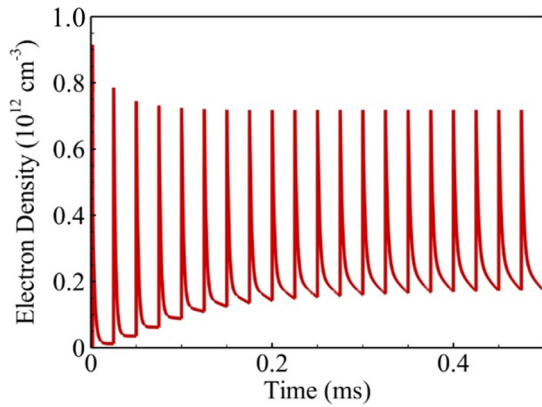


Figure 4. Temporal evolution of electron density versus time at the center of the discharge domain. Simulation conducted in H₂/air mixture at 114 Torr and 473 K initial pressure and temperature, respectively, at 40 kHz repetition rate [24]. Reproduced from [24]. © IOP Publishing Ltd. All rights reserved.

The transport equation of electron number density and the Poisson equation for electric potential are strongly coupled, which results in a severe time-step restriction. To handle this issue without affecting the accuracy, a semi-implicit form of the Poisson equation [65] is solved using the implicit lower upper (LU) factorization method. The transport equations of electron number density and electron energy density are time-advanced using an implicit generalized minimal residual (GMRES)-based ODE solver [66].

Under repeated nanosecond discharge, the electrical characteristics (input energy, E/N , n_e , etc) of the non-equilibrium plasma present quasi-periodic behaviors, as shown in figure 4. Taking advantage of this behavior, the electrical characteristics do not need to be re-calculated every pulse, which significantly reduces computation time. More importantly, the stiffness of the system can be reduced dramatically, and the stringent time step size of O (0.1–1 ps) during each pulse can be relaxed to O (0.1–1 ns). Detailed evaluations [24, 29] show that the electrical characteristics are not exactly periodic but approach quasi-periodicity after a certain number of pulses. After the plasma has reached this quasi-equilibrium, the input energy per pulse saturates to a constant value, thus the accumulated input energy is linearly proportional to the number of pulses. Based on this observation, a ‘frozen electric field’ strategy [24] is implemented.

This strategy contains three steps. First, several discharge pulses are simulated based on the full model, until $\Delta n_{e,\max} \leq 5\%$. Second, the temporal-spatial distributions of E/N , n_e , and n_e during the first pulse reaching $\Delta n_{e,\max} \leq 5\%$ are saved in a look-up table. Last, in all the following pulses, the Poisson equation for ϕ and the transport equations of n_e and n_e are turned off, with the values of E/N , n_e , and n_e frozen at the values in the table. In most cases, approximately 10 pulses are adequate to reach the quasi-equilibrium. Therefore, the speed-up factor from this strategy is approximately a tenth of the total number of pulses. The accuracy of this strategy has been verified and validated for a wide range of conditions [24].

3.2. Correlated dynamic adaptive chemistry and transport (CO-DACT) strategy

A fractional time-step Strang-splitting scheme [67] is employed to separate the convection–diffusion terms and the

chemical source terms in the transport equations of neutral and ion species. The convection–diffusion terms are time-advanced using an explicit 4th-order Runge–Kutta method. The chemical source terms are time-advanced implicitly using the classical variable coefficient stiff ODE solver (VODE) [68]. The subroutines for the plasma chemistry mechanism are generated from an open-source 0D plasma kinetics solver, ZDPlasKin [69]. Numerical diagnostics indicate that more than half of the computation time is spent on the implicit time-integration of chemical source terms. To tackle this issue, several acceleration techniques are proposed and employed with extensive verification [25].

Firstly, the point-implicit stiff ODE solver (ODEPIM) [25, 70–73], a semi-implicit solver, is employed to replace the purely implicit VODE solver. Providing similar accuracy, ODEPIM is approximately 60 times faster than VODE.

Since the computation time for chemistry is (linearly to cubically) proportional to the number of species, a dynamic adaptive chemistry (DAC) [74] technique is proposed. DAC generates a locally reduced kinetics mechanism for each spatial location and time step. Only the reaction rates of selected species and reactions are calculated, and the rest are frozen. To reduce the large computational overhead for local mechanism reduction, a correlated version of DAC (CO-DAC) [25, 71–73, 75] is proposed to create time-space correlation zones with similar thermo-chemical states, with only one time local reduction needed for each zone. CO-DAC is eminently suitable for the problems shown in figure 1, because of the uniformity of the bulk plasma and the quasi-periodic behaviors of the discharge. CO-DAC further speeds up the chemistry calculation by a factor of approximately 3 with negligible computational overhead.

Equipped with ODEPIM and CO-DAC, the dynamic evaluation of mixture-averaged transport coefficients (viscosity, thermal conductivity, and species diffusivity) becomes a large portion of the total computation time. Using the same correlation technique as in DAC but different zone grouping criteria [25, 71, 72, 76], the calculation of mixture-averaged transport coefficients is reduced by more than 800 times with negligible computational overhead.

3.3. Three-stage multi-time scale modeling strategy

Plasma-assisted ignition and combustion take place over a broad range of time scales. The ionization wave propagation, electrical breakdown, cathode sheath formation, and electron impact reactions have characteristic time scales at the sub-nanosecond level. Fast gas heating from the quenching of excited species and ion recombination has characteristic time scales on the order of microseconds. The cumulative effects of repetitive pulses, convective and diffusive transport, and ignition and combustion, occur in the range from milliseconds to seconds.

In nanosecond pulsed plasma discharges, the sub-nanosecond scale physical processes occur within each pulse. The microsecond level processes occur primarily during gaps between adjacent pulses. The millisecond to second scale processes occur generally after the accumulation of a significant number of pulses. To utilize this decoupling of time scales, a two-level adaptive time-step approach [23, 77] is proposed,

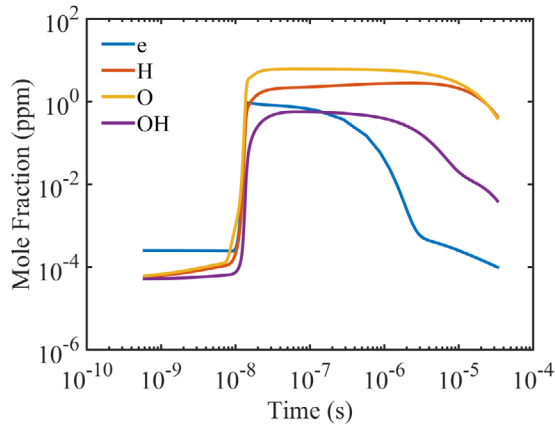


Figure 5. Time evolution of electron, H, O, and OH during 1st discharge pulse and 1st period (between beginning of 1st pulse and beginning of 2nd pulse) at center of domain. Simulation conducted in $C_2H_4/O_2/Ar$ mixture at 60 Torr initial pressure and 300 K initial temperature, at 30 kHz repetition rate [29].

and it is extended to a three-level version for computationally efficient simulation of ignition [57].

During each voltage pulse, all equations are solved simultaneously, and the time step size is set to O (0.1–1 ps). The exact time step size is dynamically determined based on the strength of E/N , the electron number density, and the Courant–Friedrichs–Lewy (CFL) condition for convection–diffusion terms.

In the duration between two consecutive pulses, both applied and gap voltages are nearly zero. As a result, the charge density quickly vanishes, and the electric field and its influence become negligible. The Poisson equation for electric potential and the electron energy equation are turned off, and the electric field and total charge are set to zero. This significantly reduces the stiffness of the system, such that the time step size can be increased to O (0.1–1 ns) without sacrificing accuracy or triggering numerical instability. The time step size is reset to O (0.1–1 ps) at the start of the following pulse, and this procedure is repeated until all pulses are finished.

After all pulses are completed, the time step of O (0.1–1 ns) is still too small to reach ignition in times on the order of 1–1000 ms within a reasonable computation time. To handle this issue, the transport equations of all charged species (electrons and ions) are turned off to further reduce the stiffness, so that the time step could be further increased to O (10–100 ns) [57] without sacrificing accuracy or triggering numerical instability.

4. General theory

In this section, a general theory of plasma-assisted ignition and combustion is established, based on results from high-fidelity modeling and simulations. The framework consists of three components. The first component is a multi-time scale theory for nanosecond pulsed plasma discharges. The second component is a theory of plasma-assisted ignition, including one- and two- stage ignition, and the propagation of the ignition kernel. The last component is a theory of plasma-assisted flames, including both premixed and non-premixed flames.

4.1. Nanosecond pulsed plasma discharges: a multi-time scale theory

Previous studies [23, 29, 30, 37, 77, 78] on the nanosecond pulsed plasma discharge of air and fuel/oxidizer/diluent mixtures have provided very detailed information about the underlying physical processes. Here we establish a general theory of nanosecond discharges based on existing literature and our model results.

Because of the multiscale nature of plasma, it is convenient to differentiate the key physical processes based on their characteristic times. The characteristic time scale τ_k for the decay of the k th species can be estimated as

$$\tau_k = - \left[\frac{\partial}{\partial Y_k} \left(\frac{dY_k}{dt} \right) \right]^{-1} = \left(\frac{\partial \text{Dec}_k}{\partial Y_k} \right)^{-1} \quad (22)$$

where the decay rate Dec_k is defined as the rate sum of all reactions with the k th species as a reactant [79]. As an example, the temporal decay of electrons, H, O, and OH radicals is shown in figure 5 to indicate the different ranges of time scale involved. Since physical time scales depend on pressure (collision rates), the pressure range is specified as 60–150 Torr. The pulsed discharges in this study have discharge durations of O (10 ns) and frequencies of 10–100 kHz. The gap between two adjacent pulses is of O (10–100 μ s), and O (100) pulses could finish within a few ms.

The multi-time scale theory for nanosecond pulsed plasma discharges is summarized in table 1. The underlying physical processes are categorized into four stages with drastically different time scales. The first stage is the discharge pulse, which has time scales of O (1–10 ns). The second stage is the afterglow phase in the gap between two adjacent pulses, which has time scales of O (100 ns). The third phase is the remaining gap between pulses, which has time scales of O (1–100 μ s). The fourth stage is the completion of O (100) pulses, which has time scales of O (1–1000 ms). Details of the physical processes in each stage will be discussed in the following sections.

4.1.1. Stage I—discharge pulse. During this stage, the discharge pulse deposits electrical energy into the gas mixture, which becomes the source of the non-equilibrium plasma. The energy deposition depends primarily on the ionization rate of the background gas. For most mixtures of fuel/oxidizer/diluent, the normal background gases are oxidizer and diluent, because of the low concentration of fuel (typically a few percentage by mole-fraction). Therefore, a change of fuel type has very limited influence on the energy deposition [37]. For a fixed peak voltage V_{peak} , the electrical energy deposition per pulse Q_{pulse} is linearly proportional to the capacitor current, which is equal to the capacitance times the time rate of change in voltage ($V_{\text{peak}}/t_{\text{pulse}}$) across the capacitor. In particular, based on a parametric study for V_{peak} from 10 kV to 90 kV, Nagaraja and Yang [37] proposed that for a pressure of 50 Torr and an initial gas temperature of 300 K,

$$Q_{\text{pulse}} = 0.14 (V_{\text{peak}}/t_{\text{pulse}}) + 0.64. \quad (23)$$

Q_{pulse} is also proportional to pressure and thus particle number density, but only a weak function of pulsing frequency [23]. In

Table 1. Multi-time scale theory for nanosecond pulsed plasma discharges.

Time scales (60–150 Torr)	Stage (10–100 kHz)	Key processes and mechanisms	Oxidizer and diluent	Fuel	Gas heating
O (1–10 ns)	Discharge pulse	Primary breakdown (60–75% of input energy coupling) Fast ionization → uniform discharge Electron impact reactions (no T_{gas} dependence)	Excitation (>50% of input energy) Electron impact dissociation: $\text{O}_2 \rightarrow \text{O} + \text{O} (^1\text{D})$	H abstraction → H (re-activate LTC) dissociation	Electron impact dissociation Vibrational relaxation
O (100 ns)	Afterglow	e-ion recombination Quenching of excited species (weak T_{gas} dependence)	Dissociation via quenching of excited species: $\text{O}_2 \rightarrow \text{O} + \text{O} (^1\text{D})$	dissociation	Fast gas heating (0.5–2 K per pulse)
O (1–100 μs)	Remaining gap between pulses	Chain propagation & termination (sensitive to T_{gas})	$\text{O}_2 + \text{fuel fragment} / \text{H} \rightarrow \text{HO}_2$ $\text{O}/\text{OH} + \text{HO}_2 \rightarrow \text{O}_2 + \text{OH}/\text{H}_2\text{O}$ O/OH + fuel: • H abstraction → OH/H ₂ O • dissociation or pyrolysis • Partial oxidation		Exothermic chain termination
O (1–1000 ms)	O (100) pulses or after all pulses	Slow/weak process (sensitive to T_{gas}) Convection & diffusion Cumulative effects of multiple pulses (weak T_{gas} dependence)	• $\text{O} + \text{O}_2 + \text{M} \leftrightarrow \text{O}_3 + \text{M}$ • dissociation or pyrolysis • Partial oxidation • $\text{CO} \rightarrow \text{CO}_2$ Large pool of radicals & fuel fragments (enhance/re-activate LTC)		exothermic O_3/CO formation & partial oxidation Uniform T_{gas} profile, volumetric heating

contrast, the range of E/N depends strongly on pulsing frequency [78]. More precisely, as shown in figure 6, higher frequency has lower peak value for the primary spike but higher peak values for the secondary spikes. This is because higher pulsing frequency increases the residual electron density and serves as a uniform pre-ionization source, which lowers the breakdown voltage.

Figure 7 shows that vibrational excitation dominates the input energy coupling when E/N is smaller than ~ 100 Td, while electronic excitation dominates when E/N is greater than ~ 100 Td [23]. For this reason, secondary spikes in the E/N profile represent pure vibrational energy coupling, and higher frequency pushes more input energy into vibrational excitation, which quickly relaxes and contributes to the fast gas heating for bulk plasma [80].

During the high voltage pulse, the fast ionization wave during the primary breakdown (60–75% of input energy coupling [23, 27, 29]) results in nearly uniform plasma discharge. The charge surge inside the sheath layers form a strong shield, which makes V_{gap} and the electric field in the bulk plasma drop almost immediately after breakdown (figure 2). As shown in figure 3, the electric field inside the sheath layers continues to increase with further increase in applied voltage, which results in rapid ion Joule heating inside the sheath layers (30–40 K within 80 ns) [23]. Under the high E/N inside the sheath layers, the electrons are accelerated significantly to fly out of the sheath layers into the bulk plasma with high energies of 10–100 eV [26].

The large number of high-energy electrons triggers ultra-fast electron impact reactions, which are the most important processes in this stage. Electron impact reactions are not dependent on gas temperature, and this is partially why

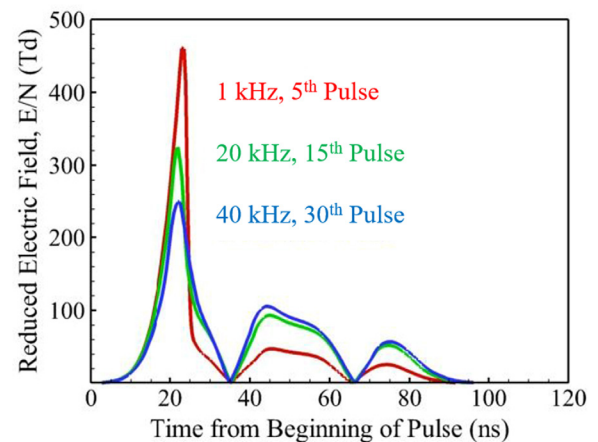


Figure 6. Temporal evolution of E/N during a nanosecond voltage pulse at different repetition rates after the discharge process has attained a periodic steady state. Simulation conducted in air at 60 Torr initial pressure and 300 K initial temperature [78]. Reproduced with permission [78]

plasma can trigger/sustain low-temperature ignition/combustion. These reactions can be classified into two categories: electron impact excitation and electron impact dissociation. The former one uses more than half of the input energy [26] and efficiently generates electronically excited O_2 and N_2/Ar species, including $\text{O}_2(a^1\Delta)$, $\text{O}_2(b^1\Sigma)$, $\text{O}_2(c^1\Sigma)$, $\text{N}_2(A^3\Sigma)$, $\text{N}_2(B^3\Pi)$, $\text{N}_2(C^3\Pi)$, $\text{N}_2(a^1\Sigma)$, Ar^* . In most cases, the concentration of diluent (N_2/Ar) is higher than O_2 , so the concentration of excited N_2/Ar is also higher than that of excited O_2 . Electron impact dissociation reactions dissociate O_2 into O , $\text{O} (^1\text{D})$, and $\text{O} (^1\text{S})$, which contributes 40–70% of O generation and part of

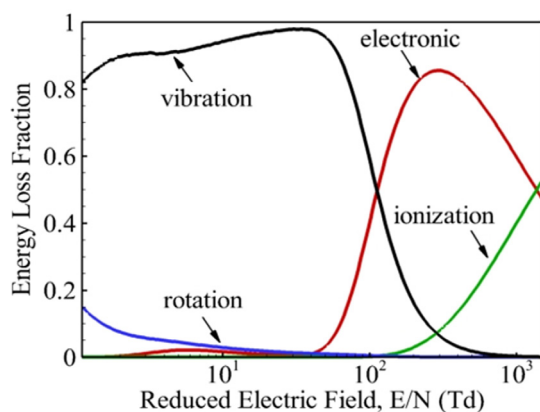


Figure 7. Fraction of electron energy lost in excitation of internal energy modes and ionization of O_2 and N_2 molecules in air as a function of E/N [23]. Reproduced from [23]. © IOP Publishing Ltd. All rights reserved.

the fast gas heating in bulk plasma [23, 29]. $O + O(^1D)$ is the dominant product combination of the electron impact dissociation of O_2 [62]. Electron impact can also dissociate N_2 into N and $N(^2D)$ [56], but the rates of these dissociation reactions are significantly lower than those of O_2 because of the strong triple bond in N_2 . The electron impact on fuel molecules can trigger H-abstraction and dissociation/pyrolysis of fuel. The electron impact reaction dissociates H_2 fuel into two H radicals, which partially replaces the original chain initiation reactions in classical H_2 combustion kinetics with high activation energies [37]. The electron impact reactions abstract H from C_2H_4 fuel molecules to produce fuel fragments C_2H_3 and C_2H_2 , and this contributes more than half of the H radical generation [29]. For fuels with LTC, electron impact reactions abstract H from fuel molecule RH (for example, fuel radical R is C_7H_{15} for n-heptane, and is CH_3OCH_2 for DME) to produce R and H radicals, which can re-activate LTC for initial gas temperatures higher than the typical LTC threshold temperature (such as 800 K at a reduced pressure of 76 Torr) [34, 57].

The fast reactions between $O(^1D)$ and fuel can result in further H-abstraction and dissociation/pyrolysis of fuel molecules, which are approximately 4 times faster than the quenching of $O(^1D)$ to O radical [29]. For H_2 fuel, a low-temperature chain propagation reaction $O(^1D) + H_2 \rightarrow OH + H$ is introduced, which is more than two orders of magnitude faster than the classical chain propagation reaction $O + H_2 \rightarrow OH + H$ and dominates the OH radical production for the first few pulses [37]. For C_2H_4 fuel, the H-abstraction reaction $C_2H_4 + O(^1D) \rightarrow C_2H_3 + OH$ produces approximately 25% of OH radical generation; the dissociation reactions $C_2H_4 + O(^1D) \rightarrow CH_2 + CH_2O$ and $C_2H_4 + O(^1D) \rightarrow CH_3 + HCO$ produce 63% of CH_2 , 17% of CH_2O (a typical marker species for LTC), 60% of CH_3 , and 20% of HCO [29]. For fuels with typical LTC, $O(^1D)$ abstracts H from fuel molecule RH to produce R and OH radicals, which contributes more than half of the $O(^1D)$ consumption [30, 34].

4.12. Stage II—afterglow. Quenching of $N_2(A^3\Sigma, B^3\Pi, C^3\Pi, a^1\Sigma)$ or Ar^* from Stage I further dissociates O_2 into O, $O(^1D)$, and $O(^1S)$, which contributes approximately 60% or 30% of O production, respectively [23, 29]. This indicates that either the production rate of excited N_2 is larger than that of excited Ar, or

the excited N_2 is more active than excited Ar. In addition, $O + O(^1D)$ is the dominant product during the dissociation of O_2 from quenching of excited diluent species. This quenching is approximately 4 times slower than the reactions between O_2 and fuel molecules in Stage I [29]. The quenching also introduces several new NO_x formation pathways: $N_2(A^3\Sigma) + O \rightarrow NO + N(^2D)$ and $N(^2D) + O_2 \rightarrow NO + O$ [56]. Although linearly proportional to the number of discharge pulses [53, 56], the amount of NO_x introduced by these new pathways is significantly smaller than the decrease in NO_x from the plasma-assisted ultra-lean combustion [5]. The quenching can also result in fuel dissociation/pyrolysis. In particular, the quenching of $N_2(A^3\Sigma)$ can dissociate H_2 into 2H, which partially replaces the original chain initiation reactions in classical H_2 combustion kinetics with high activation energies [37]. Quenching of the excited species is the major source for fast gas heating of 0.5–2 K per pulse inside the bulk plasma [27, 78, 80], and consumes 20–40% of the discharge energy [29, 80].

In this stage, in addition to quenching, there is conversion of one excited species into another excited species. The major conversion pathways are $O(^1S) \rightarrow O(^1D)$ and $O_2(c^1\Sigma) \rightarrow O_2(b^1\Sigma) \rightarrow O_2(a^1\Delta)$ [29].

As shown in figure 5, the electron-ion recombination reactions have a time scale of O (100 ns) [26, 29], which is defined as the time for electron number density to reach its initial levels, thus occur primarily in this stage. Electron-ion recombination reactions contribute part of the fast gas heating of the bulk plasma, and some of them may trigger further decomposition: $e + O_2^+/N_2^+ \rightarrow 2O/2N$ [26]. Reactions in this stage have only weak gas temperature dependence, which is partially why plasma can trigger and sustain low-temperature ignition and combustion.

4.13. Stage III—remaining gap between pulses. In the third stage, O_2 reacts with fuel fragments (such as HCO) or H radical to generate HO_2 , one of the most important species for LTC. For hydrogen fuel, the three-body reaction $H + O_2 + M \rightarrow HO_2 + M$ is the primary source of HO_2 [27]. For hydrocarbon fuels, this reaction is still primary source under high pressures, but $HCO + O_2 \rightarrow CO + HO_2$ becomes the primary source of HO_2 and CO under low pressures (that is, ~90% of HO_2 and >80% of CO under 60 Torr) [29]. HO_2 is quasi-stable and reacts significantly slower than the other radicals at low gas temperatures, so its reactions occur primarily in this stage. Highly exothermic radical reactions with HO_2 ($O/OH + HO_2 \rightarrow O_2 + OH/H_2O$) are significantly faster than those with fuel molecules, and dominate the OH radical production after approximately 0.1 ms (that is, after a few pulses) and contributes part of the gas heating in the bulk plasma [27, 37]. In addition, the reaction rates of radicals with HO_2 are proportional to pressure, but insensitive to equivalence ratio [24]. HO_2 also plays a role in NO_x conversion and generates more OH radical: $NO + HO_2 \rightarrow NO_2 + OH$ [56].

In this stage, gas temperature sensitive reactions between radical and fuel further contribute the H-abstraction, dissociation/pyrolysis, partial oxidation, and thus part of the gas heating in the bulk plasma. For C_2H_4 fuel, reactions between O and C_2H_4 include both H-abstraction ($O + C_2H_4 \rightarrow H + CH_2CHO$) and dissociation ($O + C_2H_4 \rightarrow CH_3 + HCO$), both of which are

also partial oxidation and release heat to the bulk plasma. Under high-pressure or low-temperature, reaction with C_2H_4 fuel consumes most of the OH radical, and the product CH_2CH_2OH is quasi-stable [29]. For fuels with typical LTC, radicals (O/H/OH) abstract H from fuel molecule RH to produce R and OH/ H_2/H_2O , and release heat to the bulk plasma, contributing approximately 50% of the consumption of O radical, and most production and consumption of OH radical [30, 34].

Over the time scales of O (1 μ s), the increase in gas temperature inside the sheath layers from the ion Joule heating in Stage I is rapidly dissipated, mainly to the cold electrode wall through heat conduction [23, 80]. This dissipation prevents the overheating of the sheath layers and the development of ionization instabilities.

4.1.4. Stage IV—completion of O (100) pulses. Under low pressures, the conversion between O and O_3 via $O + O_2 + M \leftrightarrow O_3 + M$ is a relatively slow process, and can equal or exceed the production rate of O only at time scales of O (ms) [23]. In addition, the decay of O_2 ($a^1\Delta$) and O_2 ($b^1\Sigma$) is even slower than the formation and decomposition of O_3 , on the order of O (1 s) and O (10 ms), respectively [29]. For combustion systems, in which plasma and flame are spatially decoupled (that is, not *in situ*), the relatively long lifetimes of O, O_3 , and O_2 ($a^1\Delta$) under low pressures makes them important carriers of the enhancement from plasma [26]. First, the plasma zone generates large amounts of O, O_3 , and O_2 ($a^1\Delta$). Then, the flow transports these species to the preheat zone of the flame. Finally, the high gas temperatures in the preheat zone decompose O_3 to generate more O radical, which significantly shortens the auto-ignition delays in the preheat zone and stabilizes the flame under ultra-lean conditions.

For C_2H_4 fuel, the CH_2CHO produced from Stage III can further react with O_2 to dissociate into CO, CH_2O , and OH, which contributes approximately 40% of OH radical generation [29]. Under low gas temperatures and short time scales, more than half of CO_2 production comes from $CH_2 + O_2 \rightarrow CO_2 + (H + H, H_2)$ [17, 29], rather than from the highly exothermic chain propagation oxidation reaction $CO + OH \rightarrow CO_2 + H$, which is too weak and slow under such conditions [37].

Convection and diffusion processes also occur in this stage.

At the end of approximately 100 pulses with time scales of O (1 ms), a large pool of radicals and fuel fragments has been formed in the bulk plasma, accumulated from all the processes of Stages I-III [23], and a uniform ‘hat-shaped’ gas temperature profile has been developed. Since most of processes have weak gas temperature dependence or are even independent of gas temperature, plasma can trigger and sustain low-temperature ignition and combustion under ultra-lean combustion conditions.

4.2. Plasma-assisted ignition

Previous studies on plasma-assisted ignition [24, 27, 34, 56, 57, 80] provide detailed information about the underlying physical processes. For fuels with LTC, when the initial gas temperature is low enough, ignition takes place in two stages:

first stage ignition to ‘cool flame’, and second stage ignition to hot flame [34]. For fuels without LTC, there is no first stage ignition or ‘cool flame’, and ignition is equivalent to the second stage. After second stage ignition, the ignition kernel propagates to form a relatively stable flame front. Thus, the physical processes can be divided into three stages: first stage ignition, second stage ignition, and the propagation of ignition kernel. The general theory for plasma-assisted ignition is summarized in table 2. The details of the physical processes of each stage will be discussed in the following sections. The pressure range of the present study is specified as 60–150 Torr, and the pulsed discharges have durations of O (10 ns) and frequencies of 10–100 kHz.

4.2.1. First-stage ignition to ‘cool flame’. Two-stage ignition and ‘cool flame’ are only present in fuels with LTC, such as DME and n-heptane. First stage ignition to ‘cool flame’ occurs through a self-sustaining exothermic LTC chain branching cycle (figure 8) [34]. The fuel molecule can be expressed as RH, where R is its corresponding fuel radical (R is CH_3OCH_2 for DME, and C_7H_{15} for n-heptane). First, H abstract reactions via radicals (such as O, H, OH) generate fuel radical R. Then, R reacts with O_2 to form RO_2 , which then isomerizes to hydroperoxy alkyl radical QOOH, where Q is the corresponding alkyl radical (Q is CH_2OCH_2 for DME, and C_7H_{14} for n-heptane). After that, QOOH adds another O_2 to form O_2QOOH . Finally, O_2QOOH isomerizes and decomposes to two OH radicals, which complete the chain branching cycle.

For initial gas temperatures below ~ 700 – 800 K, as shown in figure 9, the first stage ignition to ‘cool flame’ can occur without plasma. Therefore, the plasma enhancement has a catalytic effect and depends only weakly on the number of pulses [56]. Plasma initiates a small amount of seed radicals, such as O, H and OH, at the beginning, and this accelerates the H abstraction reactions from fuel molecules and triggers the self-accelerating LTC feedback loop. This significantly reduces (approximately 10 times) the induction time of the cycle. In this case (for a small number of pulses), the plasma enhancement of LTC is nearly independent of equivalence ratio. It is more pronounced at lower gas temperatures (550–650 K) because of the difficulty of initial radical production at low gas temperature conditions, where the LTC is stronger [56].

For initial gas temperatures above ~ 700 – 800 K, as shown in figure 9, there is no first stage ignition or ‘cool flame’ without plasma. This is because direct decomposition of fuel radical R into small alkenes (the yellow and red pathways in figure 8) is significantly accelerated at higher initial gas temperatures, and the LTC chain branching cycle, which has weak gas temperature dependence, is negligible. However, plasma discharges introduce ultra-fast H-abstraction reactions $e/O(^1D) + RH \rightarrow R + (H + e)/OH$ to produce a large amount of R orders of magnitude faster than regular H-abstractions via radicals [57]. Due to the limited decomposition rate of R, a significant amount of R goes to the LTC cycle again, and the first stage ignition to ‘cool flame’ reappears, as shown in figure 9. The strength of this re-activated LTC cycle is linearly proportional to the accumulative input energy, as is the ‘cool flame’ temperature [57].

Table 2. General theory for plasma-assisted ignition.

Stage	Fuel type	Stage initial T	Stage flame T	$\tau_{\text{self}}/\tau_{\text{plasma}}$	Key processes and mechanisms
1st stage ignition to 'cool flame'	Fuels with LTC (e.g. DME, n-heptane)	>~700–800 K <~700–800 K	Linear function of input energy & initial T	$+\infty$ Exponential function of input energy	Plasma \rightarrow e, O (¹ D), O, H, and OH \rightarrow ultra-fast H-abstraction of fuel \rightarrow exothermic LTC chain branching positive feedback cycle
(2nd stage) ignition to hot flame	Fuels with LTC	1st stage ('cool flame') T	~Adiabatic flame T	Exponential to 'cool flame' T & input energy after 1st stage	Fast gas heating (0.5–2 K per pulse)
	Fuels without LTC	>Self-auto-ignition T		Exponential function of input energy	Plasma/LTC \rightarrow radicals \rightarrow exothermic T-sensitive chain branching positive feedback cycle: <ul style="list-style-type: none"> • HO₂ \rightarrow H₂O₂ \rightarrow 2OH • Fuel dissociation or pyrolysis • Fuel oxidation
		Between plasma & self- auto-ignition T		$+\infty$	
		<Plasma auto-ignition T	<Plasma auto-ignition T	No ignition	
Ignition kernel propagation	All fuel types	Plasma \rightarrow lower auto-ignition T	~Flame T uniformly	$S_{\text{ign}} \gg S_L$:diffusion not dominant	Plasma \rightarrow local radical generation & preheating (smaller MIE)

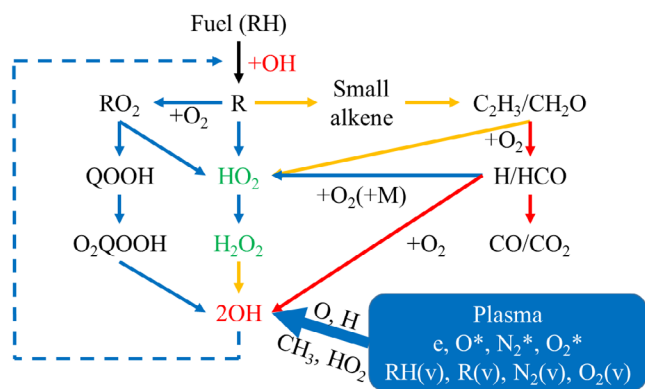


Figure 8. Schematic of the key reaction pathways for plasma-assisted fuel oxidation at different gas temperatures (blue arrow below 700 K; yellow arrow 700–1050 K; red arrow above 1050 K). Note that critical gas temperature conditions are pressure dependent. e: energetic electrons, *: electronically excited molecules; v: vibrationally excited molecules [34]. [34] 2016 © Springer Science+Business Media New York 2015. With permission of Springer.

For all gas temperature ranges, when the number of pulses is large (approximately 50 pulses or more), plasma enhancement is more than just a catalytic effect, and the relationship between 'cool flame' temperature and accumulative input energy is linear even when the initial gas temperature is below ~700–800 K. In this case, the normalized first stage ignition rate $\tau_{\text{self}}/\tau_{\text{plasma}}$ (the reduction factor of the first stage ignition delay) is an exponential function of accumulative input energy [57]. The reason for this is that the reactivity to generate radicals and excited species is an exponential function of electron temperature at low gas temperatures, which is linearly proportional to input electrical energy. In this case, the reduction of the first stage ignition delay is significantly larger than in the pure catalytic case; for

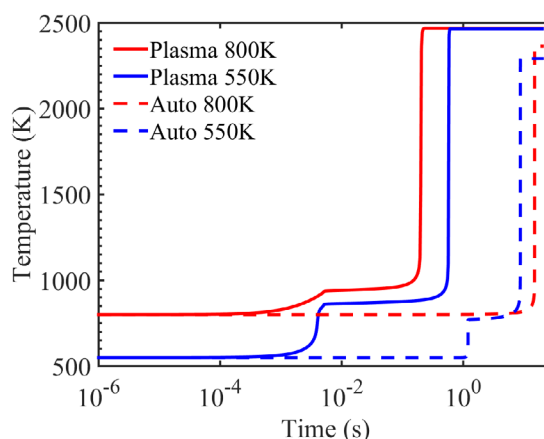


Figure 9. Comparison of gas temperatures for plasma-assisted stimulation (30 kHz repetition rate) and auto-ignition of DME/O₂/Ar mixture at 76 Torr pressure [57].

example, 150 pulses reduce ignition delay by approximately 250 times for a DME/O₂/Ar mixture at 76 Torr [57].

4.2.2. Second-stage ignition to hot flame. The concept of the second-stage ignition is relevant to the two-stage ignition of fuels with LTC; the ignition of fuels without LTC can be considered as the second stage ignition. This stage can be further divided into two steps. In the first step, the gas-heating sources increase the gas temperature to beyond a threshold value (auto-ignition temperature). Below this threshold gas temperature, ignition will not occur because of the competition between quenching and radical production. In the second step, above the threshold gas temperature, chain branching and fuel oxidation pathways are triggered and accelerated until the process becomes self-sustaining, and the gas temperature continues to rise until the final ignition. For this reason,

during this second step, the effect of plasma is negligible [27]. A threshold value exists because typical chain branching reactions are endothermic and highly gas temperature sensitive. A small increase in gas temperature near ignition significantly increases the chain branching reaction rates to produce radicals, which then accelerates the heat release from fuel oxidation. Consequently, the radical profiles are much steeper than their gas temperature counterpart. The increase in gas temperature completes the cycle by further increasing the rates of chain branching reactions. This non-linear positive feedback cycle causes an exponential increase in both gas temperature and radical concentrations, subsequently leading to ignition.

The presence of plasma can reduce the threshold auto-ignition temperature and enhance or shorten the first step but not the second step. For example, at pressures of 80–100 Torr, plasma reduces the auto-ignition temperature of lean H_2 /air mixtures (equivalence ratios of 0.06–0.12) from ~ 900 K to ~ 700 K, as shown in figure 10 [27]. As described in previous sections, fast gas heating of 0.5–2 K per pulse takes place in the bulk plasma, primarily from the quenching of excited species. In addition, the large pool of radicals and excited species generated by the plasma or the LTC chain branching cycle pre-activates the high-temperature chain branching and oxidation pathways (such as $2HO_2 \rightarrow H_2O_2 + O_2$ and $H_2O_2 \rightarrow 2OH$), which also release a large amount of heat. For a given type of nanosecond pulsed discharge, there exists a threshold number of pulses, or equivalently a threshold accumulative input energy, to trigger ignition. Plasma is thus seen to have a larger enhancing effect in the first stage [56, 57], where it can have catalyst effects, while the second stage depends on threshold-like behavior. For two-stage ignition of fuels with LTC, if the number of pulses after the first stage is small (20–30 pulses), then the radical pool directly introduced by plasma will be much smaller than that introduced by the LTC cycle of the ‘cool flame’. In that case, a plasma burst after the first stage provides predominantly thermal enhancement, which only reduces the second stage ignition delay by approximately 30% [56].

As shown in figure 10, the ignition delay increases steeply as the number of pulses is reduced. The normalized ignition rate $\tau_{self}/\tau_{plasma}$ (reduction in ignition delay) is an exponential function of accumulative input energy [27], because reactivity is an exponential function of electron temperature at low gas temperatures, and an exponential function of gas temperature at high gas temperatures, both of which are linearly proportional to input electrical energy. For fuels with LTC, this relation is equivalent to an exponential function of both ‘cool flame’ temperature and the accumulative input energy after the first stage [57], because the former one is linearly proportional to the latter one. When the number of pulses is small (within ~ 10 pulses), the discharge pulses applied at the beginning have negligible impact on the ‘cool flame’ temperature, and thus negligible impact on the second stage ignition delay [56]. In contrast, when the number of pulses is large (approximately 50 pulses or more), the LTC chain branching cycle is either significantly enhanced or re-activated, which generates a significantly larger radical pool and heat release than the un-enhanced or un-activated cycle and significantly reduces the second stage ignition delay. Taking a $DME/O_2/Ar$ mixture under 76 Torr and 150 discharge pulses as

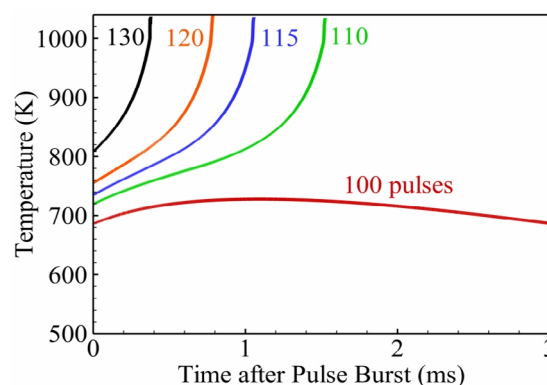


Figure 10. Temporal evolution of gas temperature at center of discharge volume. Initial pressure and gas temperature are 80 Torr and 473 K, respectively (H_2 /air mixture, CPT pulser, 40 kHz) [27]. Reprinted from [27], Copyright 2014, with permission from Elsevier.

an example [57], for initial gas temperatures below ~ 700 – 800 K, the LTC chain branching cycle is only enhanced, so the ignition time reduction factor is only ~ 15 . For initial gas temperatures above ~ 700 – 800 K, the LTC chain branching cycle is re-activated, so the reduction factor could be as large as ~ 75 .

4.2.3. Ignition kernel propagation. Auto-ignition first occurs at the center of the discharge gap, where the gas temperature first reaches the reduced threshold value [27]. Nevertheless, assisted by plasma discharges, the gas temperature profile is close to uniform distribution [23, 29], such that other locations also reach the reduced threshold gas temperature rapidly (indeed, almost simultaneously). Auto-ignition occurs independently at different locations because the local preheated mixture is doped with radicals from the plasma discharge burst [80], such that heat transport does not play a significant role [27]. This is different from hot-spot thermal igniters, which require diffusion of both radicals and heat [80]. As a result, the ignition kernel expands rapidly to the entire volume, except near the quasi-isothermal walls, where the rapid heat conduction losses from the high gas temperature gradients keep the gas temperature low [23, 29]. Therefore, the plasma-assisted ignition kernel propagation speed is significantly faster than laminar flame speed (approximately 15 times faster for lean H_2 /air mixture at 80 Torr), and plasma can ignite the entire volume of premixed mixture significantly faster than thermal ignition but with smaller minimum ignition energy (MIE) [80].

4.3. Plasma-assisted flames

Previous studies on plasma-assisted flames investigated the two basic flame types: premixed [28] and non-premixed (diffusion) flames [26]. All other (practical) flames are combinations of these two basic flame types, so the plasma enhancement on them can be inferred. These studies provide detailed information about the underlying physical processes; here we summarize the findings to develop general theories for both types.

4.3.1. Premixed flame. In this study, due to the limitations of the 1D model, we only consider the laminar flat premixed flame, which is enhanced by *in situ* plasma discharges, as

Table 3. General theory for plasma-assisted premixed flame.

Zone	Near the burner		Pre-heat zone	Post-flame zone
T range	<~500 K		~500–700 K	~700 K—flame T
ρ & N			High	Low
E/N range			~100–700 Td	~700–1500 Td
Dominant mode			Electronic	Ionization
Input energy			~10%	~90%
Non-equilibrium plasma chemistry	O ₃	O ₂ + O + M → O ₃ + M	O ₃ (+M) → O ₂ + O (+M)	Electron impact ionization does NOT contribute to radical production
• Spatially uniform	HO ₂	H + O ₂ + M → HO ₂ + M	O/OH + HO ₂ → O ₂ + OH/H ₂ O	
• Gradient ↑	O		Increase by a factor of ~6	
	H		Increase by a factor of ~4	
	OH		Increase by ~100–500%	Increase by ~40%
Direct gas heating	A significant portion of plasma enhancement			
Enhancement for T	Increase by ~20%; gradient ↑			

shown in figure 1(b). The premixed flame contains several zones: the pre-heat, reaction, and post-flame zones. In the laminar premixed flame, the reaction zone is very thin, so the volumetric plasma enhancement is not significant there. Near the burner, due to fast heat conduction to the wall, the gas temperature is lower than ~500 K, and several quasi-stable species are formed and last. Based on these analyses, we organize the general theory for plasma-assisted premixed flame into three zones: near the burner zone, pre-heat, and post-flame zones, which is summarized in table 3.

Figure 11 shows the spatial distributions of E/N , electron number density, OH concentration, and gas temperature in the presence of a lean premixed H₂/O₂/N₂ flame. E/N varies inversely with N (proportional to the gas temperature at a constant pressure condition) during each pulse. Because of intense gas expansion from heat release, high E/N (~700–1500 Td) regions are found downstream of the flame (in the high-temperature flame and post-flame zones). Inside the cathode sheath (near the boundary of the post-flame zone), E/N attains its highest value of approximately 1500 Td for a short duration. In this range, as shown in figure 7, a significant fraction of the input energy goes to ionization, and thus less electron energy can go to electronic mode to generate radicals via electron impact reactions. In contrast, lower E/N values (100–700 Td) in the low gas temperature pre-heat zone and near the burner push more energy into the electronic mode, which promotes more electron impact excitation and dissociation to generate radicals and excited species in an efficient manner. In figure 11(b), as a direct comparison, plasma increases OH concentrations by ~100–500% in the pre-heat zone, but only by ~40% in the post-flame zone. The largest increase of ~500% occurs near the burner surface. Increased OH concentrations enhance the heat release from the primary chain propagating oxidation reactions (OH + H₂/CO → H₂O/CO₂ + H). The resulting increase in gas temperature accelerates the conventional fuel oxidation chain branching, creating a positive feedback loop for radical production. With plasma discharge, gas temperatures increase by approximately 20% in both the pre-heat and post-flame zones, as shown in figure 11(b). Such difference in gas temperature could be attributed to the heat release triggered

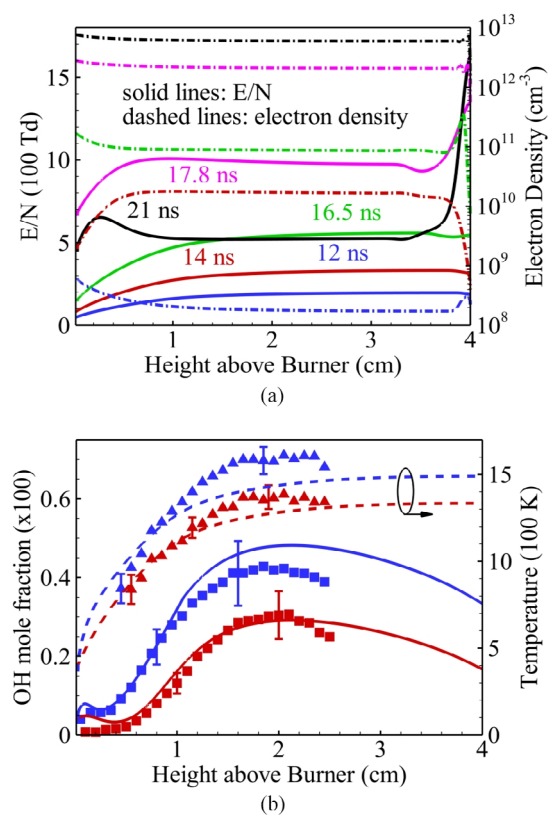


Figure 11. Spatial distributions of (a) E/N and electron number density, and (b) measured and predicted OH concentration (squares) and gas temperature (triangles) (red: without plasma; blue: with plasma), at 25 Torr in a H₂/O₂/N₂ flame (equivalence ratio = 0.5) [28]. Reprinted from [28], Copyright 2015, with permission from Elsevier.

by partial oxidation of fuel molecules by plasma-generated radicals. Effects of both chemistry and direct gas heating are responsible for a significant portion of the plasma enhancement. In fact, non-equilibrium plasma generates considerably larger amounts of radicals than the same rate of indiscriminate gas heating. The plasma chemistry enhancement of the flame is more pronounced at fuel-lean conditions.

In the pre-heat zone, plasma discharges significantly increase O and H radicals, with the peak values increasing by factors of six and four, respectively. In addition, as shown

Table 4. General theory for plasma-assisted non-premixed (diffusion) flame.

Zone	T	Chemistry
Discharge	Initial T	Afterglow: $O_2 + O + M \rightarrow O_3 + M$
Oxidizer tube exit	Plasma \rightarrow preheated T	Only long lifetime species survive: O, O_3 , $O_2(a^1\Delta)$
Radical production zone: shift upstream	Preheated T—flame T	$O_3 (+M) \rightarrow O_2 + O (+M)$ rapidly; $O_2(a^1\Delta) \rightarrow O_2$ rapidly; only O survives
Flame zone: shift upstream towards the oxidizer tube exit	Flame T \uparrow (dominant) \Rightarrow rapid fuel consumption: breakup, chain branching, oxidation ($OH + H_2/CO \rightarrow H_2O/CO_2 + H$)	O enhances chain branching: $O + H_2 \rightarrow OH + H$; $O + H_2O \rightarrow 2OH \Rightarrow OH\uparrow$ ~ 10 times (larger at low p)

in figure 11(b), gradients of radical concentrations and gas temperature are also substantially higher. Both species and gas temperature profiles shift upstream toward the burner (approximately 0.2 cm) at low plasma power, suggesting that plasma accelerates auto-ignition in the pre-heat zone. Joule heating alone could not move the gas temperature and species profiles as far upstream as the pulsed plasma source of the same total power. Closer to the burner, the low gas temperature enhances the formation of O_3 and HO_2 via three-body reactions from O and H radicals, respectively. O_3 travels a short distance downstream until its decomposition when the gas temperature rises to ~ 500 K. HO_2 persists for a longer distance, until the gas temperature increases to above ~ 700 K. In summary, non-equilibrium chemistry effects are of critical importance in the lower-temperature regions upstream of the flame.

In this configuration, only $\sim 10\%$ of the total input energy is coupled in the pre-heat and reaction zones, while $\sim 90\%$ of the total input energy is coupled in the post-flame zone, which does not enhance the pre-heat zone. To increase the energy coupled in the pre-heat zone, it has been proposed that the high-voltage electrode should be placed closer to the flame, which will require that the material to tolerate higher temperatures.

4.3.2. Non-premixed (diffusion) flame. In this study, a counter-flow diffusion flame is employed at pressures ranging from 60 to 300 Torr, with the oxidizer stream enhanced by plasma discharges. As shown in figure 1(c), this configuration can be divided into four zones: the plasma discharge zone inside the oxidizer tube, the region near the oxidizer tube exit, the radical production zone between the oxidizer tube exit and the flame, and the flame zone. Based on this analysis, a general theory for a plasma-assisted non-premixed (diffusion) flame is developed, and summarized in table 4.

In this configuration, the plasma discharges are not *in situ* with respect to the flame, so only species with long lifetimes of O (1 ms), mainly including O, O_3 , and $O_2(a^1\Delta)$, can reach the oxidizer tube exit. Among them, O_3 is primarily generated in the afterglow by three-body recombination $O_2 + O + M \rightarrow O_3 + M$. At higher pressures, the recombination rates of plasma generated radicals increase such that fewer radicals could survive to reach the flame zone. In addition, plasma discharges also pre-heat the oxidizer flow to higher gas temperature.

In the radical production zone, due to the higher gas temperature, O_3 rapidly decomposes to O_2 and O radical, and $O_2(a^1\Delta)$ rapidly quenches to O_2 . As a result, only O radical can reach the flame to provide enhancement from plasma.

Following this, the OH radical increases by approximately 10 times in the flame zone, primarily through chain branching reactions of $O + H_2 \rightarrow OH + H$ and $O + H_2O \rightarrow 2OH$. This increase in OH radical, together with the higher oxidizer flow temperature, results in rapid fuel consumption in the flame zone, including breakup, chain branching, and oxidation ($OH + H_2/CO \rightarrow H_2O/CO_2 + H$). In addition, the peak flame temperature also rises noticeably with plasma activation.

If the flame location is identified by maximum temperature location, then plasma shifts both the radical production zone and flame location toward the oxidizer tube exit. Plasma also significantly increases the extinction strain rates by more than two times, to sustain stable lean combustion.

5. Conclusions

An integrated theoretical/numerical framework for plasma-assisted ignition and combustion is reviewed. Three physical configurations are considered to cover ignition and premixed and non-premixed flames. A two-temperature model is employed for non-equilibrium plasma. It is found that modeling must be at least 1D to capture cathode sheath formation, and to calculate E/N accurately. The plasma-combustion chemistry mechanisms for a wide range of fuel types are examined to illustrate how to develop such mechanisms from existing air-plasma chemistry and fuel combustion chemistry.

Modeling strategies are explored and summarized. The ‘frozen electric field’ strategy utilizes the quasi-periodic behaviors of the electrical characteristics to avoid re-calculation during each pulse. To deal with the intense calculation of large and stiff chemistry and the evaluation of associated transport properties, a point-implicit stiff ODE solver (ODEPIM) and correlated dynamic adaptive chemistry and transport (CO-DACT) strategy are employed. CO-DACT generates locally reduced kinetics mechanisms for each spatial location and time step. Only the reaction rates of selected species and reactions are calculated, while the rest are frozen to reduce the chemistry calculation. A three-stage multi-time scale modeling strategy takes advantage of the separation of time scales in nanosecond pulsed plasma discharges to dynamically adjust the time step size for simulations.

A general theory of plasma-assisted ignition and combustion is developed. The theory has three major components: a multi-time scale theory for nanosecond pulsed plasma discharges, a theory for plasma-assisted ignition, and theories for plasma-assisted premixed and non-premixed flames.

A multi-time scale theory for nanosecond pulsed plasma discharge sets the foundation of plasma enhancement for ignition and combustion; it can be divided into four stages based on the time scales of the underlying physical processes. Stage I is the discharge pulse, which has time scales of O (1–10 ns). In this stage, most input energy is coupled into electron impact excitation and dissociation reactions, to generate a large amount of excited species and radicals under low gas temperatures. Stage II is the afterglow phase during the gap between two adjacent pulses, and has time scales of O (100 ns). Quenching of excited species is the primary physical process in this stage. It not only further dissociates both O₂ and fuel molecules to generate radicals under low gas temperatures, but also provides fast gas heating. Stage III is the remainder of the gap between two adjacent pulses, with time scales of O (1–100 μs). The radicals generated during Stages I and II significantly enhance the exothermic chain propagation and termination reactions in this stage. Stage IV takes place after a large number of pulses, with time scales of O (1–1000 ms). This stage includes weak and slow reactions, convective and diffusion transport, and the cumulative effects of multiple pulses, including preheated gas temperatures and a large pool of radicals and fuel fragments.

Plasma-assisted ignition can be divided into three stages: the first stage ignition to ‘cool flame’ (only for fuels with LTC), the second stage ignition to hot flame, and the ignition kernel propagation. In the first stage, plasma generates a large amount of e, O (¹D), O, H, and OH, enhancing the H-abstraction of fuel molecules, which in turn either significantly enhances (below ~700–800 K) or re-activates (above ~700–800 K) the exothermic LTC chain branching positive feedback cycle. In the second stage, the radicals from the first stage trigger and enhance the exothermic high gas temperature chain branching cycle, which leads to ignition of hot flames. The acceleration of ignition is a function of input energy. The ignition kernel propagation is close to auto-ignition triggered by radicals and pre-heating at different locations; it is much faster than laminar flame speed and requires lower input energy than purely thermal ignition.

For premixed and non-premixed flames, plasma could significantly enhance the radical generation and gas heating in the pre-heat zone, thereby leading to ultra-fast auto-ignition and/or flashback.

Acknowledgments

This work was supported partly by the William RT Oakes Endowment of the Georgia Institute of Technology, and partly by MURI research grant FA9550-09-0602 from the Air Force

Office of Scientific Research, with Dr. Chiping Li as technical monitor. Wenting Sun acknowledges the AFOSR award FA-9550-16-1-0441.

ORCID iDs

Suo Yang  <https://orcid.org/0000-0002-9924-2645>

References

- [1] Starikovskiy A and Aleksandrov N 2013 Plasma-assisted ignition and combustion *Prog. Energy Combust. Sci.* **39** 61–110
- [2] Lefkowitz J K, Guo P, Ombrello T, Won S H, Stevens C A, Hoke J L, Schauer F and Ju Y 2015 Schlieren imaging and pulsed detonation engine testing of ignition by a nanosecond repetitively pulsed discharge *Combust. Flame* **162** 2496–507
- [3] Cathey C D, Tang T, Shiraishi T, Urushihara T, Kuthi A and Gundersen M A 2007 Nanosecond plasma ignition for improved performance of an internal combustion engine *IEEE Trans. Plasma Sci.* **35** 1664–8
- [4] Singleton D, Pendleton S J and Gundersen M A 2011 The role of non-thermal transient plasma for enhanced flame ignition in C₂H₄-air *J. Phys. D: Appl. Phys.* **44** 022001
- [5] Pilla G, Galley D, Lacoste D A, Lacas F, Veynante D and Laux C O 2006 Stabilization of a turbulent premixed flame using a nanosecond repetitively pulsed plasma *IEEE Trans. Plasma Sci.* **34** 2471–7
- [6] Ombrello T, Won S H, Ju Y and Williams S 2010 Flame propagation enhancement by plasma excitation of oxygen. Part I: effects of O₃ *Combust. Flame* **157** 1906–15
- [7] Ombrello T, Won S H, Ju Y and Williams S 2010 Flame propagation enhancement by plasma excitation of oxygen. Part II: effects of O₂ (a¹Δ_g) *Combust. Flame* **157** 1916–28
- [8] Lacoste D, Moeck J, Durox D, Laux C and Schuller T 2013 Effect of nanosecond repetitively pulsed discharges on the dynamics of a swirl-stabilized lean premixed flame *J. Eng. Gas Turbines Power* **135** 101501
- [9] Zhang S, Sobota A, Van Veldhuizen E and Bruggeman P 2014 Gas flow characteristics of a time modulated APPJ: the effect of gas heating on flow dynamics *J. Phys. D: Appl. Phys.* **48** 015203
- [10] Zhang S, Sobota A, van Veldhuizen E and Bruggeman P 2015 Temporally resolved ozone distribution of a time modulated RF atmospheric pressure argon plasma jet: flow, chemical reaction, and transient vortex *Plasma Sources Sci. Technol.* **24** 045015
- [11] Kim W, Do H, Mungal M G and Cappelli M A 2008 Optimal discharge placement in plasma-assisted combustion of a methane jet in cross flow *Combust. Flame* **153** 603–15
- [12] Starikovskaia S 2006 Plasma assisted ignition and combustion *J. Phys. D: Appl. Phys.* **39** R265
- [13] Leonov S B, Yarantsev D A, Napartovich A P and Kochetov I V 2006 Plasma-assisted combustion of gaseous fuel in supersonic duct *IEEE Trans. Plasma Sci.* **34** 2514–25
- [14] Leonov S B and Yarantsev D A 2007 Plasma-induced ignition and plasma-assisted combustion in high-speed flow *Plasma Sources Sci. Technol.* **16** 132
- [15] Uddi M, Jiang N, Mintusov E, Adamovich I V and Lempert W R 2009 Atomic oxygen measurements in air and air/fuel nanosecond pulse discharges by two photon laser induced fluorescence *Proc. Combust. Inst.* **32** 929–36

- [16] Yin Z, Adamovich I V and Lempert W R 2013 OH radical and temperature measurements during ignition of H₂-air mixtures excited by a repetitively pulsed nanosecond discharge *Proc. Combust. Inst.* **34** 3249–58
- [17] Lefkowitz J K, Uddi M, Windom B, Lou G F and Ju Y 2015 *In situ* species diagnostics and kinetic study of plasma activated ethylene pyrolysis and oxidation in a low temperature flow reactor *Proc. Combust. Inst.* **35** 3505–12
- [18] Ventzek P L, Hoekstra R J and Kushner M J 1994 Two-dimensional modeling of high plasma density inductively coupled sources for materials processing *J. Vac. Sci. Technol. B* **12** 461–77
- [19] Shigeta M 2016 Turbulence modelling of thermal plasma flows *J. Phys. D: Appl. Phys.* **49** 493001
- [20] Yin Z, Montello A, Carter C D, Lempert W R and Adamovich I V 2013 Measurements of temperature and hydroxyl radical generation/decay in lean fuel-air mixtures excited by a repetitively pulsed nanosecond discharge *Combust. Flame* **160** 1594–608
- [21] Lefkowitz J K, Guo P, Rousso A and Ju Y 2015 Species and temperature measurements of methane oxidation in a nanosecond repetitively pulsed discharge *Phil. Trans. R. Soc. A* **373** 20140333
- [22] Togai K, Tsolas N and Yetter R A 2016 Kinetic modeling and sensitivity analysis of plasma-assisted oxidation in a H₂/O₂/Ar mixture *Combust. Flame* **164** 239–49
- [23] Nagaraja S, Yang V and Adamovich I 2013 Multi-scale modelling of pulsed nanosecond dielectric barrier plasma discharges in plane-to-plane geometry *J. Phys. D: Appl. Phys.* **46** 155205
- [24] Nagaraja S and Yang V 2014 A ‘frozen electric-field’ approach to simulate repetitively pulsed nanosecond plasma discharges and ignition of hydrogen-air mixtures *J. Phys. D: Appl. Phys.* **47** 385201
- [25] Yang S, Yang V, Sun W, Nagaraja S, Sun W, Ju Y and Gou X J 2016 Parallel on-the-fly adaptive kinetics for non-equilibrium plasma discharges of C₂H₄/O₂/Ar mixture *54th AIAA Aerospace Sciences Meeting (AIAA 2016-0195)* (<https://doi.org/10.2514/6.2016-0195>)
- [26] Nagaraja S and Yang V 2011 Nanosecond plasma enhanced counterflow diffusion flames *42nd AIAA Plasmadynamics and Lasers Conf. (AIAA 2011-3448)* (<https://doi.org/10.2514/6.2011-3448>)
- [27] Nagaraja S, Yang V, Yin Z and Adamovich I 2014 Ignition of hydrogen-air mixtures using pulsed nanosecond dielectric barrier plasma discharges in plane-to-plane geometry *Combust. Flame* **161** 1026–37
- [28] Nagaraja S, Li T, Sutton J A, Adamovich I V and Yang V 2015 Nanosecond plasma enhanced H₂/O₂/N₂ premixed flat flames *Proc. Combust. Inst.* **35** 3471–8
- [29] Yang S, Gao X, Yang V, Sun W, Nagaraja S, Lefkowitz J K and Ju Y 2016 Nanosecond pulsed plasma activated C₂H₄/O₂/Ar mixtures in a flow reactor *J. Propul. Power* **32** 1240–52
- [30] Rousso A, Yang S, Lefkowitz J, Sun W and Ju Y 2017 Low temperature oxidation and pyrolysis of n-heptane in nanosecond-pulsed plasma discharges *Proc. Combust. Inst.* **36** 4105–12
- [31] Starikovskii A Y, Anikin N B, Kosarev I N, Mintousov E I, Nudnova M M, Rakitin A E, Roupasov D V, Starikovskaia S M and Zhukov V P 2008 Nanosecond-pulsed discharges for plasma-assisted combustion and aerodynamics *J. Propul. Power* **24** 1182–97
- [32] Sun W and Ju Y 2013 Nonequilibrium plasma-assisted combustion: a review of recent progress *J. Plasma Fusion Res.* **89** 208–19 (http://www.jspf.or.jp/Journal/PDF_JSPF/jspf2013_04/jspf2013_04-208.pdf)
- [33] Ju Y and Sun W 2015 Plasma assisted combustion: dynamics and chemistry *Prog. Energy Combust. Sci.* **48** 21–83
- [34] Ju Y, Lefkowitz J K, Reuter C B, Won S H, Yang X, Yang S, Sun W, Jiang Z and Chen Q 2016 Plasma assisted low temperature combustion *Plasma Chem. Plasma Process.* **36** 85–105
- [35] Takashima K, Yin Z and Adamovich I V 2012 Measurements and kinetic modeling of energy coupling in volume and surface nanosecond pulse discharges *Plasma Sources Sci. Technol.* **22** 015013
- [36] Li T, Adamovich I V and Sutton J A 2013 A burner platform for examining the effects of non-equilibrium plasmas on oxidation and combustion chemistry *Combust. Sci. Technol.* **185** 990–8
- [37] Nagaraja S and Yang V 2012 Chemical and transport effects of nanosecond plasma discharges on H₂-Air and C₂H₄-air mixtures *50th AIAA Aerospace Sciences Meeting (AIAA 2012-0382)* (<https://doi.org/10.2514/6.2012-382>)
- [38] Sun W, Uddi M, Ombrello T, Won S H, Carter C and Ju Y 2011 Effects of non-equilibrium plasma discharge on counterflow diffusion flame extinction *Proc. Combust. Inst.* **33** 3211–8
- [39] Mostaghimi J, Proulx P and Boulos M I 1987 A two-temperature model of the inductively coupled rf plasma *J. Appl. Phys.* **61** 1753–60
- [40] Davoudabadi M, Shrimpton J S and Mashayek F 2009 On accuracy and performance of high-order finite volume methods in local mean energy model of non-thermal plasmas *J. Comput. Phys.* **228** 2468–79
- [41] Hagelaar G and Pitchford L 2005 Solving the Boltzmann equation to obtain electron transport coefficients and rate coefficients for fluid models *Plasma Sources Sci. Technol.* **14** 722–33
- [42] Macheret S O, Shneider M N and Miles R B 2002 Modeling of air plasma generation by repetitive high-voltage nanosecond pulses *IEEE Trans. Plasma Sci.* **30** 1301–14
- [43] Wang Q, Economou D J and Donnelly V M 2006 Simulation of a direct current microplasma discharge in helium at atmospheric pressure *J. Appl. Phys.* **100** 023301
- [44] Incropera F D, Bergman D and Lavine T A 2007 *Fundamentals of Heat and Mass Transfer* (New York: Wiley) (<http://www.wiley.com/WileyCDA/WileyTitle/productCd-EHEP001810.html>)
- [45] Wang J C and Springer G S 1973 Vibrational relaxation times in some hydrocarbons in the range 300–900 K *J. Chem. Phys.* **59** 6556–62
- [46] Feng I A and Lee M C 1982 Measurement of vibrational relaxation time of oxygen between 475° and 675° K using an acoustic resonant technique *J. Acoust. Soc. Am.* **71** 1482–6
- [47] Ionin A A, Kochetov I V, Napartovich A P and Yuryshev N N 2007 Physics and engineering of singlet delta oxygen production in low-temperature plasma *J. Phys. D: Appl. Phys.* **40** R25
- [48] Phelps A and Pitchford L 1985 Anisotropic scattering of electrons by N₂ and its effect on electron transport *Phys. Rev. A* **31** 2932
- [49] Hayashi M 2003 *Bibliography of Electron and Photon Cross Sections with Atoms and Molecules Published in the 20th Century* (Argon: National Institute for Fusion Science) (NIFS-DATA—72) (http://www.iaea.org/inis/collection/NCLCollectionStore/_Public/36/019/36019522.pdf?r=1)
- [50] Sun W, Uddi M, Won S H, Ombrello T, Carter C and Ju Y 2012 Kinetic effects of non-equilibrium plasma-assisted methane oxidation on diffusion flame extinction limits *Combust. Flame* **159** 221–9
- [51] Smith G P *et al* 1999 GRI-Mech 3.0 www.me.berkeley.edu/gri_mech/

- [52] Popov N 2008 Effect of a pulsed high-current discharge on hydrogen-air mixtures *Plasma Phys. Rep.* **34** 376–91
- [53] Uddi M, Jiang N, Adamovich I and Lempert W 2009 Nitric oxide density measurements in air and air/fuel nanosecond pulse discharges by laser induced fluorescence *J. Phys. D: Appl. Phys.* **42** 075205
- [54] Wang H, You X, Joshi A V, Davis S G, Laskin A, Egolfopoulos F and Law C K 2007 USC mech version II. High-temperature combustion reaction model of H₂/CO/C₁–C₄ compounds University of Southern California, Los Angeles, CA (http://ignis.usc.edu/USC_Mech_II.htm)
- [55] Janev R K and Reiter D 2003 Unified analytic representation of hydrocarbon impurity collision cross-sections *J. Nucl. Mater.* **313–6** 1202–5
- [56] Nagaraja S, Sun W and Yang V 2015 Effect of non-equilibrium plasma on two-stage ignition of n-heptane *Proc. Combust. Inst.* **35** 3497–504
- [57] Zhang Y, Yang S, Yang V and Sun W J 2017 Effects of non-equilibrium plasma discharge on ignition and ntc chemistry of DME/O₂/Ar mixtures: a numerical investigation *53rd AIAA/SAE/ASEE Joint Propulsion Conf. (AIAA 2017-4773)* (<https://doi.org/10.2514/6.2017-4773>)
- [58] Zhao Z, Chaos M, Kazakov A and Dryer F L 2008 Thermal decomposition reaction and a comprehensive kinetic model of dimethyl ether *Int. J. Chem. Kinet.* **40** 1–18
- [59] Seiser R, Pitsch H, Seshadri K, Pitz W and Gurran H 2000 Extinction and autoignition of n-heptane in counterflow configuration *Proc. Combust. Inst.* **28** 2029–37
- [60] Ju Y, Sun W, Burke M P, Gou X and Chen Z 2011 Multi-timescale modeling of ignition and flame regimes of n-heptane-air mixtures near spark assisted homogeneous charge compression ignition conditions *Proc. Combust. Inst.* **33** 1245–51
- [61] Hayashi M 1987 *Swarm Studies and Inelastic Electron-Molecule Collisions* ed L C Pitchford *et al* (New York: Springer) pp 167–87 (<http://www.springer.com/us/book/9781461291046>)
- [62] Capitelli M, Ferreira C M, Gordiets B F and Osipov A I 2000 *Plasma Kinetics in Atmospheric Gases* (Berlin: Springer) (<http://www.springer.com/us/book/9783540674160>)
- [63] Kurganov A and Tadmor E 2000 New high-resolution central schemes for nonlinear conservation laws and convection–diffusion equations *J. Comput. Phys.* **160** 241–82
- [64] Kulikovskiy A 1995 A more accurate Scharfetter–Gummel algorithm of electron transport for semiconductor and gas discharge simulation *J. Comput. Phys.* **119** 149–55
- [65] Arslanbekov R R and Kolobov V I 2003 Two-dimensional simulations of the transition from Townsend to glow discharge and subnormal oscillations *J. Phys. D: Appl. Phys.* **36** 2986
- [66] Hindmarsh A C, Brown P N, Grant K E, Lee S L, Serban R, Shumaker D E and Woodward C S 2005 SUNDIALS: suite of nonlinear and differential/algebraic equation solvers *ACM Trans. Math. Softw.* **31** 363–96
- [67] Kim J and Moin P 1985 Application of a fractional-step method to incompressible Navier-Stokes equations *J. Comput. Phys.* **59** 308–23
- [68] Brown P, Byrne G and Hindmarsh A 1989 VODE: a variable-coefficient ODE solver *SIAM J. Sci. Comput.* **10** 1038–51
- [69] Pancheshnyi S, Eismann B, Hagelaar G and Pitchford L 2008 *Computer Code ZDPlasKin* (Toulouse: University of Toulouse, LAPLACE, CNRS-UPS-INP) (www.zdplaskin.laplace.univ-tlse.fr)
- [70] Katta V R and Roquemore W M 2008 Calculation of multidimensional flames using large chemical kinetics *AIAA J.* **46** 1640–50
- [71] Yang S, Ranjan R, Yang V, Menon S and Sun W 2017 Parallel on-the-fly adaptive kinetics in direct numerical simulation of turbulent premixed flame *Proc. Combust. Inst.* **36** 2025–32
- [72] Yang S, Ranjan R, Yang V, Sun W and Menon S 2017 Sensitivity of predictions to chemical kinetics models in a temporally evolving turbulent non-premixed flame *Combust. Flame* **183** 224–41
- [73] Yang S, Wang X, Yang V, Sun W and Huo H J 2017 Comparison of flamelet/progress-variable and finite-rate chemistry LES models in a preconditioning scheme *55th AIAA Aerospace Sciences Meeting (AIAA 2017-0605)* (<https://doi.org/10.2514/6.2017-0605>)
- [74] Gou X, Chen Z, Sun W and Ju Y 2013 A dynamic adaptive chemistry scheme with error control for combustion modeling with a large detailed mechanism *Combust. Flame* **160** 225–31
- [75] Sun W, Gou X, El-Asrag H A, Chen Z and Ju Y 2015 Multi-timescale and correlated dynamic adaptive chemistry modeling of ignition and flame propagation using a real jet fuel surrogate model *Combust. Flame* **162** 1530–9
- [76] Sun W and Ju Y 2017 A multi-timescale and correlated dynamic adaptive chemistry and transport (CO-DACT) method for computationally efficient modeling of jet fuel combustion with detailed chemistry and transport *Combust. Flame* **184** 297–311
- [77] Poggie J, Adamovich I, Bisek N and Nishihara M 2012 Numerical simulation of nanosecond-pulse electrical discharges *Plasma Sources Sci. Technol.* **22** 015001
- [78] Nagaraja S and Yang V 2013 Energy coupling in repetitively pulsed nanosecond dielectric barrier discharges in plane-to-plane geometry *51st AIAA Aerospace Sciences Meeting (AIAA 2013-0569)* (<https://doi.org/10.2514/6.2013-569>)
- [79] Gou X, Sun W, Chen Z and Ju Y 2010 A dynamic multi-timescale method for combustion modeling with detailed and reduced chemical kinetic mechanisms *Combust. Flame* **157** 1111–21
- [80] Yang S, Nagaraja S, Sun W and Yang V J 2015 A detailed comparison of thermal and nanosecond plasma assisted ignition of hydrogen-air mixtures *53rd AIAA Aerospace Sciences Meeting (AIAA 2015-1615)* (<https://doi.org/10.2514/6.2015-1615>)